Journal Pre-proof

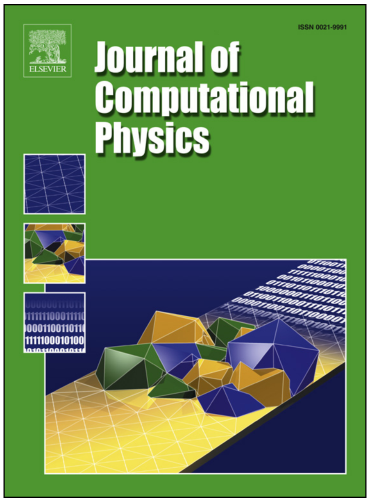

Comparison of rigorous scattering models to accurately replicate the behaviour of scattered electromagnetic waves in optical surface metrology

Helia Hooshmand, Tobias Pahl, Poul-Erik Hansen, Liwei Fu, Alexander Birk et al.

PII: S0021-9991(24)00767-8
DOI: https://doi.org/10.1016/j.jcp.2024.113519
Reference: YJCPH 113519

To appear in: *Journal of Computational Physics*

Received date: 14 June 2024
Revised date: 18 October 2024
Accepted date: 19 October 2024

Please cite this article as: H. Hooshmand, T. Pahl, P.-E. Hansen et al., Comparison of rigorous scattering models to accurately replicate the behaviour of scattered electromagnetic waves in optical surface metrology, *Journal of Computational Physics*, 113519, doi: https://doi.org/10.1016/j.jcp.2024.113519.

Highlights

- Developing rigorous models to compute scattered light from diverse surface geometries.
- Using the localised Fourier modal method for single-structure scattering.
- Evaluating model accuracy by comparing the near-field intensity with the Mie solution.
- Evaluating model adaptability by comparing scattered fields from various profile Research Highlights.

Comparison of rigorous scattering models to accurately replicate the behaviour of scattered electromagnetic waves in optical surface metrology

Helia Hooshmand[1], Tobias Pahl[2], Poul-Erik Hansen[3], Liwei Fu[4], Alexander Birk[4], Mirza Karamehmedović[5], Peter Lehmann[2], Stephan Reichelt[4], Richard Leach[1], and Samanta Piano[1]

[1] *Manufacturing Metrology Team, Faculty of Engineering, University of Nottingham, Jubilee Campus, Nottingham NG8 1BB, United Kingdom*
[2] *Measurement Technology Group, Faculty of Electrical Engineering and Computer Science, University of Kassel, Wilhelmshoeher Allee 71, 34121 Kassel, Germany*
[3] *Danish Fundamental Metrology A/S, Kogle Alle 5, DK-2970 Hørsholm, Denmark*
[4] *Institute of Applied Optics, University of Stuttgart, Pfaffenwaldring 9, 70569 Stuttgart, Germany*
[5] *Department of Applied Mathematics and Computer Science, Technical University of Denmark, DK-2800 Kgs. Lyngby, Denmark*

Abstract

Rigorous scattering models are based on Maxwell's equations and can provide high-accuracy solutions to model electromagnetic wave scattering from objects. Being able to calculate the scattered field from any surface geometry and considering the effect of the polarisation of the incident light, make rigorous models the most promising tools for complex light-matter interaction problems. The total intensity of the electric near-field scattering from a silicon cylinder illuminated by the transverse electric and transverse magnetic polarisation of the incident light is obtained using various rigorous models including, the local field Fourier modal method, boundary element method and finite element method. The intensity of the total electric near-field obtained by these rigorous models is compared using the Mie solution as a reference for both polarisation modes of the incident light. Additionally, the intensity of the total electric near-field scattered from a silicon sinusoid profile using the same rigorous models is analysed. The results are discussed in detail, and for the cylinder, the deviations in the intensity of the total electric field from the exact Mie solution are investigated.

Keywords: Light scattering, rigorous model, electric field, Maxwell's equation.

1 Introduction

Interaction between light and matter plays a crucial role in spectroscopy, optical metrology, sensing, imaging, quantum information processing and lasers [1, 2]. In optical metrology, due to the continuously increasing applications of surface texture measurement [3–5], the demand for high-quality measurement technologies increases. These technologies mainly rely on determining the elastically scattered electromagnetic field from the surface by modelling the interaction of the electromagnetic field with the matter on the surface [6]. The scattered light field is then propagated through the optical instrument to generate the image.

Modelling optical surface topography measuring instruments based on scattering models is of significant importance as it helps in understanding instrument characteristics and performance specifications, which consequently leads to optimising instrument configurations to achieve the most accurate results possible. One important aspect of optical instrument modelling is determining the instrument's response to surface height variation. Within well-defined limits, the elementary Fourier optics model [7], based on scalar diffraction theory and classical Fourier optics, is used to characterise the instrument transfer function (ITF) [8], topographic lateral resolution [9] and residual nonlinearities [10].

In general, approximate and rigorous models can be employed in order to model the scattered light field. As approximate scattering models are fast and simple approaches to calculate the scattered field, they have already been used to describe interference microscopy by propagating the scattered field through the optical instrument [11–14]. Nevertheless, approximate models have certain limitations in their ranges of validity, which restrict their application to weakly scattering media (materials whose refractive index differs only slightly from that of the surrounding medium), surfaces with relatively small height variations and/or slowly varying surfaces on the optical scale [15]. However, due to the increasing use of freeform surfaces, surfaces with technologically advanced texturing, and additively manufactured structures in engineering, aerospace industry and biology, analysing the complex features on surfaces is becoming more critical [16]. In rigorous models, the fundamental properties of light are described by Maxwell's electromagnetic theory and the laws governing the propagation of light in a medium [17]. They are necessary to calculate the scattered light from complex surface geometries containing overhangs and re-entrant features, features with small radii of curvature, or other geometries where multiple scattering occurs. Besides optical metrology, which has seen particularly widespread use of rigorous scattering models, these models are applicable in various other fields of engineering and science, such as fluid mechanics, acoustics, electromagnetics, fracture mechanics, and plasticity. Rigorous models can also account for the polarisation of the incident and scattered light, surface plasmons and near-field scattering. The behaviour of light at the interface between two different media is determined by the boundary conditions for the electromagnetic wave vectors. In nonmagnetic materials with no free charges and conduction currents, these conditions require continuity of the tangential components of the electric and magnetic fields across the boundary [18].

To predict the scattered light from complex surface geometries, various rigorous models have been proposed. Finite element methods (FEMs) [19] provide an efficient numerical approach to solve partial differential equations over complex domains using a set of boundary conditions. For the case of inhomogeneous and near-planar surface structures, such as those forming semiconductor devices, the Fourier modal method (FMM), also known as rigorous coupled wave analysis (RCWA) [20, 21], provides a semi-analytical solution. FMM is a particularly efficient way to analyse the performance of periodic structures such as blazed and lamellar diffraction gratings [22, 23]. The finite-difference time-domain (FDTD) method [24] is based on the discretisation of Maxwell's equations in space and time and has been extensively used in computational electrodynamics [25, 26]. The method of moments (MoM) [27] is a rigorous numerical technique for analysing electromagnetic radiation, scattering and wave propagation problems using the integral form of Maxwell's equations, as opposed to their differential form that is used in the FEM or FDTD methods. In computational terms, the process can be treated as a boundary element method (BEM) [28] in which elemental areas act as finite sources and radiate into the volume of interest. An accelerated variant of MoM is the method of fundamental solutions (also called the method of auxiliary sources) and related techniques [29–33], where the traditional boundary elements are replaced by Dirac delta or higher-order point sources distributed on a surface in the interior of the scattering structure.

With respect to optical metrology, the FMM and FEM models have been used to model the measurement of nano-textured surfaces using scatterometry [34, 35]. The three-dimensional (3D) BEM method, also named surface integral equation method, accelerated via the multi-level fast multipole method (MLFMM) has been used to simulate speckle field distributions [36]. The FEM, FMM and BEM methods have been employed to model coherence scanning interferometry and confocal microscopy signals [37–39]. The FEM model is used to model microsphere-enhanced microscopy and interferometry to study the lateral resolution enhancement in microscopic imaging [40, 41]. The BEM model is employed to investigate the optical surface topography measurement of steep and tilted surfaces when tilting the object at angles larger than the numerical aperture slope limit [42].

An accuracy comparison has been made among different implementations of various numerical approaches, including aperiodic-FMM (a-FMM), FEM, FDTD, the volume integral method (VIP) and a hybrid method (combination of FMM and a-FMM), all applied to a slit-groove diffraction problem [43]. A detailed comparison of the performance of some of the rigorous models in near-field scattering computations for metallic nanoparticles is provided in [44]. Effectively applying rigorous models to optical metrology problems requires a thorough understanding of their accuracy and validity range. However, limited research exists on comparing the accuracy of rigorous models across different applications in optical metrology [45–47].

Therefore, this paper provides a comparative analysis of four different rigorous models: a newly developed local field Fourier modal method (LFFMM) that does not require absorbing boundaries, two approaches based on the BEM (BEM K-H and BEM M, which are based on solving Kirchhoff-Helmholtz integral and Maxwell's equations, respectively), and the FEM method. After discussing the approaches in detail in Section 2, we compare the total electric near-fields, i.e. the summation of the incident and scattered fields obtained from each model, for transverse electric (TE) and transverse magnetic (TM) polarised incident light. We limit our discussion to isotropic and homogeneous scattering materials. For exemplary scattering structures, we consider a silicon cylinder, which allows us to compare against the analytic 2D Mie solution as a reference, and a sinusoidal profile representative of a scattering surface of high spatial frequency and curvature, where approximate models fail. In addition, sinusoidal profiles play an important role in determining the ITF of optical profilers [10]. In the context of cylindrical surfaces, besides the accuracy analysis of the rigorous scattering models by comparing their results with those from the exact Mie solution, it should be noted that cylinders and spheres of various diameters also play an important role in optical metrology e.g. for 3D transfer function measurements [48] and to consider curved measuring objects with high slope angles.

The results for all models, polarisations and structures are analysed and discussed in detail. Deviations from the reference solution and from each other are investigated. This illustrates each model's specific advantages and disadvantages and enables an assessment of each model's applicability, accuracy and robustness.

It is important to highlight that, despite the significance of time efficiency, memory usage, and convergence in numerical methods, our study refrains from comparing computational time due to the diverse specifications of the computers employed.

2 Rigorous scattering models

The interaction between incident electromagnetic waves and objects generates scattered fields that can be described through Maxwell's equations, which govern electric and magnetic field behaviour. For time-harmonic fields, these equations can be simplified to the Helmholtz equation, which describes wave propagation. The rigorous models considered in this paper are introduced briefly in the following. Note that the descriptions are related to the implementations used here and are not generally applicable to the respective method.

BEM is a powerful approach for solving scattering problems, emphasising the boundaries of objects (2D or 3D) to facilitate a thorough analysis of their interactions with incident waves. By characterising the scatterer through its surface boundaries, BEM enables field evaluations at these interfaces instead of throughout the entire volume. Maxwell's equations dictate the relationships among the incident, scattered, and total fields, ensuring that the tangential components of electric and magnetic fields comply with the required boundary conditions at the interfaces between different media. Additionally, the method employs Green's functions to transform the problem into boundary integrals, effectively reducing the dimensionality of the analysis and improving computational efficiency for complex geometries. The scattered field is modelled using the Kirchhoff Helmholtz integral and Maxwell's equations.

FEM is used to address electromagnetic scattering problems in bounded 2D domains by discretising the area into smaller elements. This allows for precise modelling of complex shapes and materials. To mitigate boundary reflections, a perfectly matched layer (PML) is used, which ensures that scattered fields are absorbed without reflections. The scattered electric field is derived from the vector wave equation, based on Maxwell's equations, and is analyzed within the defined physical domain, which includes the scattering object and its surrounding medium. The model accommodates both in-plane and out-of-plane scattering, facilitating three-dimensional illumination effects. Overall, FEM provides an accurate representation of scattering phenomena by effectively solving the boundary value problem through numerical techniques.

LFFMM is an extension of the FMM model tailored for finite or aperiodic 2D structures, using a Gaussian beam as the incident field to calculate scattering based on local field interactions. The method relies on the angular spectrum representation to decompose the Gaussian beam into plane waves. The scattered field for each of the plane waves is calculated using FMM. The FMM model provides a rigorous and numerically efficient 3D calculation of both in-plane and out-of-plane scattering for 3D illumination. By summing the scattered field from the plane waves, the method enables efficient computation of the scattered fields and subsequent analysis of the electromagnetic response.

2.1 BEM K-H

The BEM K-H model presented in this paper is a two-dimensional (2D) numerical rigorous model, i.e., limited to surfaces completely described only by a set of lateral and axial coordinates (xz-plane), assuming the surface is infinitely extended along the third dimension (y-axis) [28, 49].

Consider a boundary $\partial\mathrm{S}$ (contour in 2D) separating two homogeneous, isotropic and linear media labelled S and $\bar{\mathrm{S}}$, in the xz-plane, as shown in figure 1. We assume that the surface profile function $z = \zeta(x)$ depends only on one dimension, namely x. When an electromagnetic wave generated by an external source propagates through medium $\bar{\mathrm{S}}$, it will be scattered by the medium S. To obtain the scattered field, the Helmholtz equation [50] should be solved, and the boundary conditions need to be applied at the surface interface and infinity.

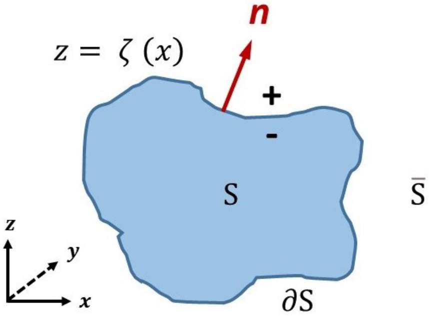

Figure 1: Geometry of the scattering object S considered for the scattering problem.

The BEM K-H model is based on the derivation of a set of coupled integral equations for the source functions, i.e. the field and its normal derivative are evaluated on the surface. With knowledge of these sources, the total field, and, thus, the solution to the scattering problem, can be obtained from the extinction theorem [18, 51] at any point above and below the surface boundary. Without loss of generality, the plane of incidence, i.e. the plane which contains the normal vector on the interface and the incident wave vector is considered in the xz-plane, and the incident light wave $\Phi^{\mathrm{inc}}(x, z, \omega)$ is either TM or TE polarised. In such a case, only the tangential component of the field (the electric field E_y for TE polarisation, and the magnetic field H_y for TM polarisation) is needed to fully describe the electromagnetic field as written below

$$\Phi_\nu(x, z, \omega) = \begin{cases} H_y(x, z, \omega) & \nu = \mathrm{TM}, \\ E_y(x, z, \omega) & \nu = \mathrm{TE}, \end{cases} \tag{1}$$

where ν describes the polarisation and ω is the angular frequency of the incident light. The fact that the primary field can be fully described by a single vector component significantly simplifies the problem, reducing it from a vector to a scalar problem. This is considered the main feature of the BEM K-H model that distinguishes this model from the BEM M model. When $\Phi_\nu(x, z, \omega)$ is known, the remaining components of the electromagnetic field can be calculated using Maxwell's equations [50]. These components, for TM polarisation, are given by

$$E_x(x, z, \omega) = -\frac{i}{\omega\varepsilon(\omega)} \frac{\partial}{\partial z} H_y(x, z, \omega), \tag{2a}$$

$$E_z(x, z, \omega) = \frac{i}{\omega\varepsilon(\omega)} \frac{\partial}{\partial x} H_y(x, z, \omega), \tag{2b}$$

where i represents the imaginary unit and $\varepsilon(\omega)$ denotes the permittivity of the medium through which the light is propagating. For TE polarisation, the remaining components are described as

$$H_x(x,z,\omega) = \frac{i}{\omega\mu(\omega)}\frac{\partial}{\partial z}E_y(x,z,\omega), \tag{3a}$$

$$H_z(x,z,\omega) = -\frac{i}{\omega\mu(\omega)}\frac{\partial}{\partial x}E_y(x,z,\omega), \tag{3b}$$

where $\mu(\omega)$ is the magnetic permeability of the medium through which the wave is propagating. Consider $\Phi_\nu(x,z,\omega)$, as described in Eq. (1), a field component that is tangential to the surface independent of the polarisation of the incident light and applying the boundary conditions at the interface $z = \zeta(x)$ leads us to [18]

$$\Phi_\nu^+(x,z,\omega)|_{z=\zeta(x)} = \Phi_\nu^-(x,z,\omega)|_{z=\zeta(x)}, \tag{4a}$$

$$\frac{1}{\kappa_\nu^+(\omega)}\partial_n\Phi_\nu^+(x,z,\omega)|_{z=\zeta(x)} = \frac{1}{\kappa_\nu^-(\omega)}\partial_n\Phi_\nu^-(x,z,\omega)|_{z=\zeta(x)}, \tag{4b}$$

where $\Phi_\nu^+(x,z)$ and $\partial_n\Phi_\nu^+(x,z)$ are the values of the field and its outward normal derivative at the outer side of the boundary ∂S, and $\Phi_\nu^-(x,z)$ and $\partial_n\Phi_\nu^-(x,z)$ at the inner side of the boundary (see figure 1). In equation (4), $\kappa_\nu^\pm(\omega)$ are defined as

$$\kappa_\nu^\pm(\omega) = \begin{cases} \varepsilon^\pm(\omega) & \nu = \mathrm{TM}, \\ \mu^\pm(\omega) & \nu = \mathrm{TE}, \end{cases} \tag{5}$$

and ∂_n denotes the normal derivative to the surface given by the following expression

$$\partial_n = \hat{\mathbf{n}}\cdot\nabla = \frac{-\zeta'(x)\partial_x + \partial_z}{\gamma(x)}, \tag{6}$$

where

$$\gamma(x) = \sqrt{1 + [\zeta'(x)]^2}. \tag{7}$$

In Eq. (6), $\partial_i \overset{i\,=\,x,\,z}{=\!=} \partial/\partial i$, $\hat{\mathbf{n}}$ is the unit normal vector on the interface directed into medium (+) (see figure 1), described by

$$\hat{\mathbf{n}} = \frac{\zeta'(x)\hat{\mathbf{x}} + \hat{\mathbf{z}}}{\sqrt{1 + [\zeta'(x)]^2}}. \tag{8}$$

According to the integral theorem of Kirchhoff-Helmholtz [52], the total field in $\bar{\mathrm{S}}$ can be presented as the surface integral

$$\Phi_\nu^{\mathrm{inc}}(\mathbf{r},\omega) + \frac{1}{4\pi}\int_{\partial\mathrm{S}}\left[\Phi_\nu(\mathbf{r}',\omega)\partial_{n'}G(\mathbf{r}-\mathbf{r}',\omega) - \partial_{n'}\Phi_\nu(\mathbf{r}',\omega)G(\mathbf{r}-\mathbf{r}',\omega)\right]d\mathrm{S}' = \begin{cases} \Phi_\nu(\mathbf{r},\omega), & \mathbf{r}\in\bar{\mathrm{S}}, \\ 0, & \mathbf{r}\notin\bar{\mathrm{S}}, \end{cases} \tag{9}$$

where $\mathbf{r} = (x,z)$, and $G(\mathbf{r}-\mathbf{r}',\omega)$ is the free-space Green's function. In 2D, an explicit representation of the outgoing, free-space Green's function is given by the Hankel function of the first kind and zeroth-order as [53]

$$G(\mathbf{r}-\mathbf{r}',\omega) = i\pi H_0^{(1)}\left(\sqrt{\epsilon(\omega)}\frac{\omega}{c}|\mathbf{r}-\mathbf{r}'|\right), \tag{10}$$

where c is the speed of light in vacuum. Similarly to equation (9), the total field in S can be written as

$$-\frac{1}{4\pi}\int_{\partial \mathrm{S}}\left[\Phi_\nu(\mathbf{r}',\omega)\partial_{n'}G(\mathbf{r}-\mathbf{r}',\omega)-\partial_{n'}\Phi_\nu(\mathbf{r}',\omega)G(\mathbf{r}-\mathbf{r}',\omega)\right]d\mathrm{S}'=\begin{cases}\Phi_\nu(\mathbf{r},\omega), & \mathbf{r}\in \mathrm{S},\\ 0, & \mathbf{r}\notin \mathrm{S}.\end{cases} \tag{11}$$

The extinction theorem considers the incident field extinguished in the region S by the induced field, as represented by the second term on the left-hand side of the equation (9). This is obtained by setting the right-hand-side of Eqs. (9) and (11) to zero [54]. Furthermore, using Eqs. (9) and (11), the field at any point (outside and inside) in the xz-plane can be found by performing a surface integral over ∂S. In order to perform this integral, however, the total field and its normal derivative on the surface boundary ∂S has to be known. Hence, in BEM, the scattering problem is equivalent to finding the field and the normal derivative on the surface.

Using Eqs. (9) and (11), the total field at the outer (+) and inner (−) side of the surface boundary can be re-written as

$$\Phi^+_\nu(\mathbf{r},\omega)=\ \Phi^{\mathrm{inc}}_\nu(\mathbf{r},\omega)\ +\ \frac{1}{4\pi}\int_{\partial \mathrm{S}}\left[\Phi^+_\nu(\mathbf{r}',\omega)\partial_{n'}G^+(\mathbf{r}-\mathbf{r}',\omega)-\partial_{n'}\Phi^+_\nu(\mathbf{r}',\omega)G^+(\mathbf{r}-\mathbf{r}',\omega)\right]d\mathrm{S}', \tag{12a}$$

$$\Phi^-_\nu(\mathbf{r},\omega)=-\frac{1}{4\pi}\int_{\partial \mathrm{S}}\left[\Phi^-_\nu(\mathbf{r}',\omega)\partial_{n'}G^-(\mathbf{r}-\mathbf{r}',\omega)-\partial_{n'}\Phi^-_\nu(\mathbf{r}',\omega)G^-(\mathbf{r}-\mathbf{r}',\omega)\right]d\mathrm{S}', \tag{12b}$$

where $G^+(\mathbf{r}-\mathbf{r}',\omega)$ and $\partial_{n'}G^+(\mathbf{r}-\mathbf{r}',\omega)$ are the Green's function and its normal derivative at the outer side the surface boundary, while $G^-(\mathbf{r}-\mathbf{r}',\omega)$ and $\partial_{n'}G^-(\mathbf{r}-\mathbf{r}',\omega)$ are the Green's function and its normal derivative at the inner side the surface boundary, correspondingly. Using Eq. (7) the surface element dS is given by the following expression

$$dS=\gamma(x)dx. \tag{13}$$

Taking the boundary conditions of Eq. (4) into account, the integral Eqs. (12) will be coupled and using Eq. (13) can be written as

$$\Phi^+_\nu(x,z,\omega)=\Phi^{\mathrm{inc}}_\nu(x,z,\omega)+\int\left[A^+(x,z|x',\omega)\mathcal{F}_\nu(x',\omega)-B^+(x,z|x',\omega)\mathcal{N}_\nu(x',\omega)\right]dx', \tag{14a}$$

$$\Phi^-_\nu(x,z,\omega)=-\int\left[A^-(x,z|x',\omega)\mathcal{F}_\nu(x',\omega)-\frac{\kappa^-_\nu(\omega)}{\kappa^+_\nu(\omega)}B^-(x,z|x',\omega)\mathcal{N}_\nu(x',\omega)\right]dx', \tag{14b}$$

where $\kappa^\pm_\nu(\omega)$ have been defined in Eq. (5), and

$$\mathcal{F}_\nu(x,\omega)=\Phi^+_\nu(x,z,\omega)|_{z=\zeta(x)}, \tag{15a}$$

$$\mathcal{N}_\nu(x,\omega)=\gamma(x)\partial_n\Phi^+_\nu(x,z,\omega)|_{z=\zeta(x)}, \tag{15b}$$

are the source functions on the surface boundary, and kernels $A^\pm(x,z|x')$ and $B^\pm(x,z|x')$ are defined as

$$A^{\pm}(x,z|x',\omega) = \frac{1}{4\pi}\gamma(x')\partial_{n'}G^{\pm}(x,z|x',z',\omega)|_{z'=\zeta(x')}, \tag{16a}$$

$$B^{\pm}(x,z|x',\omega) = \frac{1}{4\pi}G^{\pm}(x,z|x',z',\omega)|_{z'=\zeta(x')}. \tag{16b}$$

The scattered field outside and inside the scattering object is found by using Eq. (14a) and (14b), if source functions $\mathcal{F}_\nu(x,\omega)$ and $\mathcal{N}_\nu(x,\omega)$ are known. A coupled set of equations for these sources can be obtained by setting $z = \zeta(x) + \eta$ where $\eta \to 0^+$, in Eq. (14a) and (14b). Doing so results in the following set of inhomogeneous, coupled integral equations for the sources defined on the surface boundary

$$\mathcal{F}_\nu(x,\omega) = \mathcal{F}_\nu^{\rm inc}(x,\omega) + \int[\mathcal{A}^+(x|x',\omega)\mathcal{F}_\nu(x',\omega) - \mathcal{B}^+(x|x',\omega)\mathcal{N}_\nu(x',\omega)]dx', \tag{17a}$$

$$0 = \int[\mathcal{A}^-(x|x',\omega)\mathcal{F}_\nu(x',\omega) - \frac{\kappa_\nu^-(\omega)}{\kappa_\nu^+(\omega)}\mathcal{B}^-(x,|x',\omega)\mathcal{N}_\nu(x',\omega)]dx', \tag{17b}$$

where $\mathcal{F}_\nu^{\rm inc}(x,\omega)$ is the incident field at the boundary source points, and $\mathcal{A}^{\pm}(x|x',\omega)$ and $\mathcal{B}^{\pm}(x|x',\omega)$ are defined as

$$\mathcal{A}^{\pm}(x|x',\omega) = \lim_{\eta\to0^+} A^{\pm}(x,z|x',\omega)|_{z=\zeta(x)+\eta}, \tag{18a}$$

$$\mathcal{B}^{\pm}(x|x',\omega) = \lim_{\eta\to0^+} B^{\pm}(x,z|x',\omega)|_{z=\zeta(x)+\eta}. \tag{18b}$$

In order to solve Eqs. (17), the integral equations are converted into matrix equations by discretising the spatial variables x and x' using a suitable scheme to extrapolate integral points to mesh nodes [55]. Hence, the surface boundary is divided to N source points, and a system of 2N equations with 2N unknowns (N fields and N normal derivatives) is obtained by applying the integral Eqs. (17) at each point source. Once the fields $\mathcal{F}_\nu(x,\omega)$ and their normal derivatives $\mathcal{N}_\nu(x,\omega)$ are obtained at the surface boundary, the total field can be calculated at a desired point in xz-plane using Eq. (14a) and (14b).

2.2 BEM M

The second BEM model used herein is a three-dimensional (3D) rigorous simulation model [27]. In the BEM M model, the extent of the modelled object is necessarily finite in all dimensions of 3D space. This represents an important difference from the 2D models BEM K-H and FEM. While this boundary condition is usually more realistic and often advantageous in application, one has to expect some differences between the models' results due to the additional edge diffraction effects in the BEM M method. For a more in-depth explanation of the simulation, the reader is referred to previous publications on the topic [27, 36].

Since the BEM M approach is a 3D simulation, the regions S and $\bar{\rm S}$ depicted in Fig. 1 must now be considered as 3D domains and the surface ∂S as a 2D surface in a 3D space. Also, in contrast to the scalar fields in the BEM K-H model, the electric fields **E** and magnetic fields **H** are vector fields in the BEM M model. The BEM algorithm is based on the surface integral formulation of Stratton and Chu [56, 57]. In this formulation, using the vector Green's theorem, the total electric field at an arbitrary point $\mathbf{r}$ is given by

$$\mathbf{E}(\mathbf{r}) = \begin{cases} \mathbf{E}^{\mathrm{inc}}(\mathbf{r}) - \int_{\partial \mathrm{S}} \left[i\omega\mu_{\bar{S}}(\hat{\mathbf{n}} \times \mathbf{H}^{+}) G_{\bar{\mathrm{S}}} - (\hat{\mathbf{n}} \times \mathbf{E}^{+}) \times \nabla' G_{\bar{\mathrm{S}}} - (\hat{\mathbf{n}} \cdot \mathbf{E}^{+}) \nabla' G_{\bar{\mathrm{S}}} \right] \mathrm{dS}', & \mathbf{r} \in \bar{\mathrm{S}}, \\ \int_{\partial \mathrm{S}} \left[i\omega\mu_{S}(\hat{\mathbf{n}} \times \mathbf{H}^{-}) G_{\mathrm{S}} - (\hat{\mathbf{n}} \times \mathbf{E}^{-}) \times \nabla' G_{\mathrm{S}} - (\hat{\mathbf{n}} \cdot \mathbf{E}^{-}) \nabla' G_{\mathrm{S}} \right] \mathrm{dS}', & \mathbf{r} \in \mathrm{S}, \end{cases} \tag{19}$$

while the total magnetic field is given by

$$\mathbf{H}(\mathbf{r}) = \begin{cases} \mathbf{H}^{\mathrm{inc}}(\mathbf{r}) + \int_{\partial \mathrm{S}} \left[i\omega\epsilon_{\bar{S}}(\hat{\mathbf{n}} \times \mathbf{E}^{+}) G_{\bar{\mathrm{S}}} + (\hat{\mathbf{n}} \times \mathbf{H}^{+}) \times \nabla' G_{\bar{\mathrm{S}}} + (\hat{\mathbf{n}} \cdot \mathbf{H}^{+}) \nabla' G_{\bar{\mathrm{S}}} \right] \mathrm{dS}', & \mathbf{r} \in \bar{\mathrm{S}}, \\ \int_{\partial \mathrm{S}} \left[i\omega\mu_{S}(\hat{\mathbf{n}} \times \mathbf{E}^{-}) G_{\mathrm{S}} - (\hat{\mathbf{n}} \times \mathbf{H}^{-}) \times \nabla' G_{\mathrm{S}} - (\hat{\mathbf{n}} \cdot \mathbf{H}^{-}) \nabla' G_{\mathrm{S}} \right] \mathrm{dS}', & \mathbf{r} \in \mathrm{S}, \end{cases} \tag{20}$$

where $\hat{\mathbf{n}}$ is the unit normal vector on the interface pointing into $\bar{\mathrm{S}}$. $\mathbf{E}^{\pm}$ and $\mathbf{H}^{\pm}$ are the electric and magnetic fields in medium S $(-)$ and in the surrounding medium $\bar{\mathrm{S}}$ $(+)$. $G_{\bar{\mathrm{S}}}$ and G_{S} are the Green's functions in their respective domains. $\hat{\mathbf{n}}$, $\mathbf{E}^{\pm}$ and $\mathbf{H}^{\pm}$ depend on $\mathbf{r}'$, i.e. the source point on $\partial\mathrm{S}$, over which we integrate. Similarly, $G_{\bar{\mathrm{S}}}$ and G_{S} depend on the difference vector $\mathbf{r} - \mathbf{r}'$ between evaluation point and boundary element. Both dependencies are implied in Eqs. (19) and (20) for brevity. The Green's function for the 3D case is

$$G_{\Sigma}(\mathbf{r} - \mathbf{r}') = \frac{\exp(-ik_{\Sigma}|\mathbf{r} - \mathbf{r}'|)}{4\pi|\mathbf{r} - \mathbf{r}'|} \qquad \Sigma \in \{\bar{\mathrm{S}}, \mathrm{S}\} \tag{21}$$

where k_{Σ} is the wave number in the respective medium. We can see here that, due to the singularity in G_{Σ} when $\mathbf{r} \to \mathbf{r}'$, this method's accuracy is limited around $\partial\mathrm{S}$ compared to others.

The formulations in Eqs. (19) and (20) are the equivalents to (9) and (11) from the BEM K-H method, but the integrands in (19), (20) are vector valued and the integration over $\partial\mathrm{S}$ is two-dimensional. To solve for $\mathbf{E}(\mathbf{r})$ and $\mathbf{H}(\mathbf{r})$, we approximate $\partial\mathrm{S}$ using triangular elements. The surface currents on each element are expanded using Rao-Wilton-Glisson (RWG) rooftop basis functions [57]. Using the Method of Moments (MoM) approach based on Galerkin operators, the integral equations of the whole system can be expanded into the linear system of equations

$$\mathbf{x} = \mathbf{Z}\mathbf{y}, \tag{22}$$

where $\mathbf{Z}$ is the impedance matrix that represents the interactions between all basis functions and $\mathbf{x}$ and $\mathbf{y}$ are vectors of N unknowns. In general, the matrix $\mathbf{Z}$ is densely populated.

To make this method feasible for electrical large 3D structures in terms of memory footprint and computation time, we employ the multi-level fast multipole method, first described by Greengard and Rokhlin [58], and later by Song, Lu and Chew [59] for electromagnetic scattering. It harnesses the fact that, for two groups of surface elements with large spatial separation, their inter-group interactions can be approximated by the field radiating from each group which can be expanded into multipoles. This sparsifies the dense impedance matrix $\mathbf{Z}$ in Eq. (22) considerably. Together with an iterative solver like the generalised minimal residual method (GMRES) [60], it allows us to calculate systems with comparatively large surface areas of up to $60\lambda \times 60\lambda$ within a few hours (depending on convergence). This makes the comparison to the 2D methods presented herein possible.

2.3 FEM

The FEM model presented in this study is based on previous publications [37, 39], but extended to non-periodic scattering objects. For a general review of FEM in electromagnetics we refer to Jin [61] or Volakis et al. [62]. The scattering geometry, including labels of the different media and the boundary as well as the definition of the incident angles, are given in Fig. 2. Physically, the scattering object is 3D, but infinitely extended and invariant under translation in one direction (here y) as sketched in Fig. 2(a). For simulation, it is sufficient to discretize a cross-section at arbitrary y-position as outlined in Fig. 2(b). The domains S of the scattering object and $\bar{S}$ of the surrounding medium are extended by an artificial damping layer called PML to avoid reflections at the boundaries and constitute the case of an infinitely extended domain. The PML is implemented such that the scattered field enters without reflections at the interface and is damped exponentially to zero inside.

In order to obtain the scattered electric field $\mathbf{E}^{\text{sca}}$, the vector wave equation

$$\nabla \times \underline{\Lambda}^{-1} \nabla \times \mathbf{E}^{\text{sca}} - k^2 \varepsilon \underline{\Lambda} \mathbf{E}^{\text{sca}} = \mathbf{0}, \tag{23}$$

with the wave number $k = 2\pi/\lambda$ depending on the wavelength λ and the relative electric permittivity ε, which depends on the respective medium, is solved within the PML. Within the physical domain (S and $\bar{S}$), the vector wave equation

$$\nabla \times \underline{\Lambda}^{-1} \nabla \times \mathbf{E}^{\text{tot}} - k^2 \varepsilon \underline{\Lambda} \mathbf{E}^{\text{tot}} = \mathbf{0}, \tag{24}$$

with the total electric field $\mathbf{E}^{\text{tot}} = \mathbf{E}^{\text{sca}} + \mathbf{E}^{\text{inc}}$, coupled to the scattered field by the incident field $\mathbf{E}^{\text{inc}}$, is considered. Note that for incident waves restricted to the xz-plane, it is usually sufficient to solve the Helmholtz equation without further modifications, similar to the BEM K-H model as shown in a previous publication [63]. However, in this study, we focus on the vectorial modelling being able to consider out-of-plane scattering. Hence, the FEM model is a 2D model with respect to scattering objects but considers in- and out-of-plane, and therewith 3D, illumination and scattering. The PML is considered by the matrix $\underline{\Lambda}$ in Eqs. (23) and (25), which corresponds to the identity matrix in S; $\bar{S}$ and becomes complex in S_{PML} as described by Sacks et al. [64]. The damping functions of the PML are implemented to constitute an exponential damping with quadratic function of form $f(z) = \alpha_z (z - z_0)^2$ in the exponent. z_0 corresponds to the z-coordinate of the interface between the physical and PML domain. The damping constant $\alpha_z = 1$ is chosen and the thickness of the PML is given by 800 nm. The PML in x direction is implemented in exactly the same manner. Note that the PML parameters are chosen to ensure high accuracy. For a more efficient modelling, PML parameters can be adjusted to decrease the size of the PMLs. However, optimizing PML parameters is out of the scope of this paper. Therefore, for more information on PMLs, we refer to Jin [61].

In order to obtain a differential equation for the total electric field in all domains, Eq. (23) is rewritten to

$$\nabla \times \underline{\Lambda}^{-1} \nabla \times \mathbf{E}^{\text{tot}} - k^2 \varepsilon \underline{\Lambda} \mathbf{E}^{\text{tot}} = \nabla \times \underline{\Lambda}^{-1} \nabla \times \mathbf{E}^{\text{inc}} - k^2 \varepsilon \underline{\Lambda} \mathbf{E}^{\text{inc}}. \tag{25}$$

Since the scattered field is damped to zero in the PML, $\mathbf{E}^{\mathrm{tot}}(\partial S) = \mathbf{E}^{\mathrm{inc}}(\partial S)$ is chosen at the boundary ∂S.

Solving a 3D vector equation discretising a 2D area, the electric fields are split into one part parallel and the other perpendicular to the domain. Further, the relation $\mathbf{E}^{\mu}(x, y, z) = \mathbf{E}^{\mu}(x, z) \exp\left(i k_y^{\mathrm{inc}} y\right)$, $\mu = \mathrm{sca, tot, inc}$, where k_y^{inc} is the y-component of the incident wave vector

$$\mathbf{k}^{\mathrm{inc}} = \begin{pmatrix} k_x^{\mathrm{inc}} \\ k_y^{\mathrm{inc}} \\ k_z^{\mathrm{inc}} \end{pmatrix} = k \begin{pmatrix} \sin\left(\theta^{\mathrm{inc}}\right) \cos\left(\varphi^{\mathrm{inc}}\right) \\ \sin\left(\theta^{\mathrm{inc}}\right) \sin\left(\varphi^{\mathrm{inc}}\right) \\ -\cos\left(\theta^{\mathrm{inc}}\right) \end{pmatrix}, \tag{26}$$

with the incident angles θ^{inc} and φ^{inc} as sketched in Fig. 2(b), is considered to calculate y-derivatives analytically. Note that $\varphi^{\mathrm{inc}} = 0$ and $\varphi^{\mathrm{inc}} = \pi$ correspond to the 2D case where the plane of incidence corresponds to the xz-plane. The incident field is described by a plane wave $\mathbf{E}^{\mathrm{inc}} = \underline{R}(\theta^{\mathrm{inc}}, \varphi^{\mathrm{inc}})\mathbf{E}_0 \exp\left(i\mathbf{k}^{\mathrm{inc}} \cdot \mathbf{r}\right)$, where the matrix $\underline{R}$ ensures that the electric field is perpendicular to $\mathbf{k}^{\mathrm{inc}}$ and $\mathbf{E}_0$ includes the amplitude and the initial polarisation in xy-plane [37, 39].

The resulting boundary value problem is solved using the open-source software NGSolve [65]. For the parallel part of the electric field, Nédélec elements of third order are used; the vertical part is approximated by Lagrange elements of same order [66]. The geometry is discretised in triangular elements, where the maximum distance between two adjacent elements is restricted to $\lambda/(5n)$ with n being the refractive index of the respective medium.

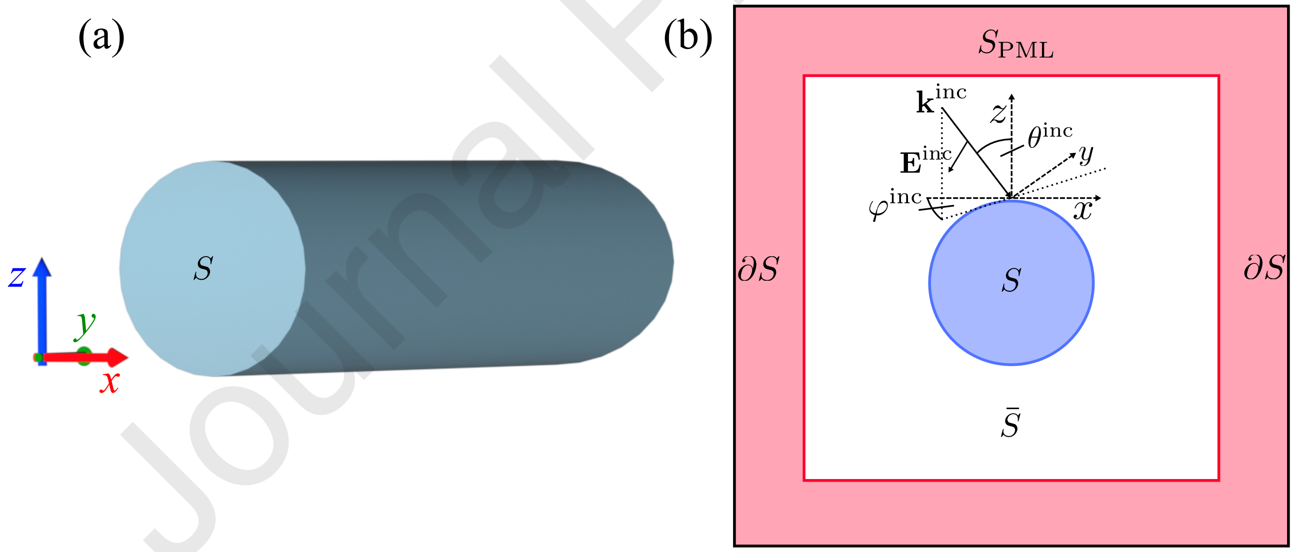

Figure 2: (a) Sketch of a 3D cylinder corresponding to the physical scattering object considered in Sec. 3.1, exemplary for a 2D scattering object. A cross-section with area S of the cylinder is used in the FEM simulation. (b) Scattering geometry for the FEM simulation with the scattering object S, the surrounding medium $\bar{S}$, and the PML medium S_{PML}. The boundary of the structure is marked by ∂S. Further, the incident angles, wave vector and electric field are sketched.

2.4 Local Field Fourier Modal Method

The FMM method is widely used for calculating the electromagnetic response from periodic structures. It is based on the Fourier plane wave decomposition of all periodic functions and has gained popularity due to its relative simplicity and efficiency for a wide class of problems.

In particular, the method is suitable for large unit cell simulation. Simulation of scattering from finite structures using the FMM may be achieved by either using absorbing boundaries or by using light confinement. In the latter case you first make a periodic implantation of the finite structure and secondly confine the incident light to one unit cell.

Here we present a method to extend the Fourier modal method to aperiodic/finite structures using field localisation. We call the method for Local field Fourier modal method (LFFMM) and use a Gaussian beam as our local field. A Gaussian beam cannot be used directly by FMM, so we need to make a plane wave decomposition (PWD) of the Gaussian field. The PWD used here is called the angular spectrum representation and it is a mathematical technique to describe optical fields in homogeneous, isotropic, linear and source-free media as a series expansion of plane waves with variable amplitudes and propagation directions. We will use the 2D PWD in reference [67, 68] for the decomposition of the incident Gaussian amplitude (E^{inc}) given by

$$E^{\text{inc}}(x, y, z = 0) = \exp\left\{-\left[\left(\frac{x}{w_{0x}}\right)^2 + \left(\frac{y}{w_{0y}}\right)^2\right]\right\}, \tag{27}$$

where w_{0x} and w_{0y} are the incident beam waist along the x and y directions, respectively.

In the angular spectrum picture, we draw a propagation axis z and consider the field at the beam waist plane ($z = 0$) transverse to the propagation direction. In this plane we can evaluated the angular spectrum $F(k_x, k_y)$ as the Fourier transform of the complex amplitude distribution E^{inc}. The Fourier transformation may replace the angular spectrum theory in the vicinity of the Gaussian beam waist since the z-component of the wave-vector is almost equal to the wave-number (k). Consequently, a Gaussian beam can be expressed as a superposition of many plane waves by the inverse Fourier transformation, which is called the angular spectrum of plane waves [69]. The process can be expressed as

$$E^{\text{inc}}(x, y, z) = \int_{-\infty}^{\infty}\int_{-\infty}^{\infty} F(k_x, k_y) \exp\left[i(k_x x + k_y y + k_z z)\right] \mathrm{d}k_x \mathrm{d}k_y, \tag{28}$$

where k_u is the wave vector component along the u ($u = x$, y or z) direction. The 2D PWD determines the plane-wave spectrum of the incident Gaussian beam by applying a 2D discrete Fourier transform. Since the incident electric field needs to be represented as a discrete set of plane waves in our implementation, we rewrite Eq. (28) as a discrete transformation. If the number of sampling points, along the direction u ($u = x$ or y), over the interval $-u_{\max} \leq u \leq u_{\max}$ is M_u, then the incident amplitude at $z = 0$ can be expressed in terms of its plane-wave spectrum as

$$E^{\text{inc}}(x, y, z = 0) = \sum_{m_x=-M_x/2}^{M_x/2-1} \sum_{m_y=-M_y/2}^{M_y/2-1} F\left(k_{x,m_x}, k_{y,m_y}\right) \exp\left[i\left(k_{x,m_x} x + k_{y,m_y} y\right)\right], \tag{29}$$

where $k_{u,m_u} = m_u \Delta_k$ is the wave vector component along the u ($u = x$ or y) direction and Δ_k is the sampling spacing. For the (m_x, m_y) sub-beam, the z wave vector component can be expressed as

$$k_{z,m_x,m_y} = \left(k^2 - k_{x,m_x}^2 - k_{y,m_y}^2\right)^{1/2}. \tag{30}$$

Therefore, each propagating component of the (m_x, m_y) sub-beam can be specified by an incident angle, an azimuth angle, and a plane-wave angular spectrum with the application of 2D PWD. Analytical integration of the normally incident Gaussian beam mode TEM_{00} in Eq. (27) is given by Eq. (31).

$$F\left(k_{x,m_x}, k_{y,m_y}\right) = \frac{w_{0x}w_{0y}}{4\pi}\exp\left\{-\left[\left(\frac{w_{0x}}{2}k_{x,m_x}\right)^2 + \left(\frac{w_{0y}}{2}k_{y,m_y}\right)^2\right]\right\}. \tag{31}$$

Parseval's theorem tells us that the integral over real space is equal to the integral over Fourier space

$$\int_{-\infty}^{\infty}\int_{-\infty}^{\infty}\left|E^{\mathrm{inc}}(x,y,z=0)\right|^2 \mathrm{d}x\mathrm{d}y = (2\pi)^2\int_{-\infty}^{\infty}\int_{-\infty}^{\infty}\left|F\left(k_{x,m_x}, k_{y,m_y}\right)\right|^2 \mathrm{d}k_x\mathrm{d}k_y. \tag{32}$$

Clearly, Eqs. (27) and (31) are bounded such that they are zero outside the intervals $[-x_{\max}, x_{\max}] \times [-y_{\max}, y_{\max}]$ and $[-k_{x,\max}, k_{x,\max}] \times [-k_{y,\max}, k_{y,\max}]$. To determine $u_{\max}$ and $k_{u,\max}$, we replace the limits of integration in Eq. (32) with finite values, choosing $\pm x_{\max}$ and $\pm y_{\max}$ large enough so that the Gaussian profile is negligible outside this region. For $\pm k_{x,\max}$ and $\pm k_{y,\max}$, we ensure that propagating modes do not exceed $2\pi/\lambda$ and adjust these values until the error in Eq. (32) is below 1×10^{-10}.

We will use the sampling spacing Δ and Δ_k along the two directions in real space and k-space. The Nyquist-Shannon sampling theorem, for one direction, requires that the following relation between the sampling spacing Δ, Δ_k and $u_{\max}$, $k_{u,\max}$ is satisfied

$$\tfrac{\pi}{\Delta} \leq k_{u,\max} \quad \tfrac{\pi}{\Delta_k} \leq u_{\max}. \tag{33}$$

In this work, we choose $\Delta = \pi/(4k_{u,\max})$ and $\Delta_k = \pi/(4u_{\max})$. The sampling points M_u may now be written as the nearest even integer of $(2u/\Delta)$. Furthermore the incident angle (θ_{m_x,m_y}) and azimuth angle (ϕ_{m_x,m_y}) of the sub-beam (m_x, m_y) are given by

$$\theta_{m_x,m_y} = \arccos\left(\frac{k_{z,m_x,m_y}}{k}\right), \tag{34}$$

$$\phi_{m_x,m_y} = \arctan\left(\frac{k_{m_y}}{k_{m_x}}\right). \tag{35}$$

If the Gaussian beam is incident at an arbitrary angle of incidence for the central beam $(m_x = m_y = 0)$ as well as an azimuth angle of the central beam, the expression for the incident wave-vector needs to be modified to

$$\mathbf{k}' = \mathbf{R}_{\theta^{\mathrm{inc}}}\mathbf{R}_{\varphi^{\mathrm{inc}}}\begin{pmatrix} k_{x,m_x} \\ k_{y,m_y} \\ k_{z,m_x,m_y}\end{pmatrix}, \tag{36}$$

where

$$\mathbf{R}_{\theta_i} = \begin{bmatrix} \cos\theta^{\mathrm{inc}} & 0 & \sin\theta^{\mathrm{inc}} \\ 0 & 1 & 0 \\ -\sin\theta^{\mathrm{inc}} & 0 & \cos\theta^{\mathrm{inc}}\end{bmatrix}, \tag{37}$$

$$\mathbf{R}_{\varphi^{\text{inc}}} = \begin{bmatrix} \cos\varphi^{\text{inc}} & \sin\varphi^{\text{inc}} & 0 \\ -\sin\varphi^{\text{inc}} & \cos\varphi^{\text{inc}} & 0 \\ 0 & 0 & 1 \end{bmatrix}. \tag{38}$$

Here, $\mathbf{k}'$ is the rotated wave-vector, θ^{inc} the angle of incident of the central beam, φ^{inc} the azimuth angle of the central beam, $\mathbf{R}_{\theta^{\text{inc}}}$ and $\mathbf{R}_{\varphi^{\text{inc}}}$ are rotational matrices.

2.4.1 Single structure calculation

The near-field and far-field from a single structure are calculated by using the periodic FMM method from reference [34]. FMM relies on solving Maxwell's equations inside a medium that is uniform in the z-direction (normal to the surface) so that the light propagating in the medium can be regarded as plane waves and subsequently performing Fourier expansion of Maxwell's equation along the x- and y-directions. Analytical treatment of the wave equation in the z-direction enables FMM to model uniform structures, with homogeneous material properties, of arbitrary heights. General structures, that are not uniform or do have altering material properties in the z-direction, are subdivided into layers with homogeneous material that are uniform in the z-direction. A necessary requirement for a good layer representation is that the integral over the permittivity and permeability for the layer representation is equal to the integral over the design structure for the same parameter. In the following procedure, we describe how to set up the FMM simulation region (1-2), how to calculate the near field for one of the sub-beams in the series expansions of plane waves (3) and finally how to add up the sub-beams in the series expansion (4).

1. Determine $u_{\max}$ and $k_{u,\max}$ using Parseval's theorem.
2. Set the FMM pitch greater than $2u_{\max}$ and set the number of modal modes high enough to ensure far field convergence [70].
3. Calculate the near field for all incident and azimuth angles of the sub-beams. Each sub-beam field is multiplied with the associated angular spectrum amplitude $F(k_{x,m_x}, k_{y,m_y})$ obtained from Eq. (31). The calculation of the field for a sub-beam is divided into three regions: the reflected region ($z < 0$), the structure layer ($0 \leq z \leq L$) and the transmitted layer $z > L$. The field in the reflected and transmitted region may be calculated using the standard Rayleigh expansion. The calculation of the field inside the structured layer depends on the FMM implementation. The most common methods are the S-matrix [71] and the enhanced transmittance matrix approach [72] used here. Further information on the implementation is given elsewhere [73–75].
4. Apply the superposition principle to obtain the resulting field from the sub-beams fields.

The advantage of the presented LFFMM method with Gaussian beam illumination is that it does not require any rewriting of the periodic FMM code and may thus be used together with any commercial periodic FMM implementation. Another advantage is that you can obtain the far-field in the same way by exchanging the near-field for the sub-beams with the far-field for the sub-beams in the above procedure. This is in contrast to the aperiodic FMM in reference [76] that requires the implementation of PML layers in the periodic FMM code and a near- to far-field transformation [77].

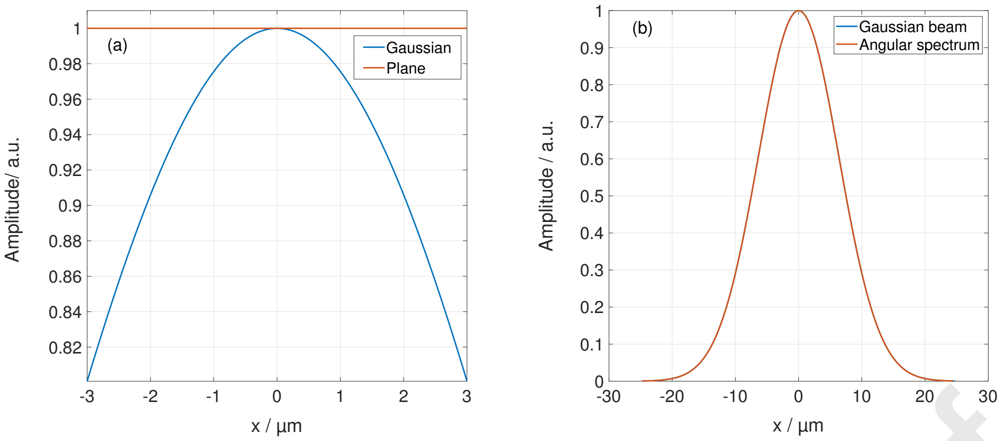

Figure 3: (a) Gaussian and plane wave amplitude over a computational grid of $[-3, 3]$ μm. (b) The Gaussian beam and its angular spectrum representation obtained using Eq. (27) and Eq. (29) respectively, underlying the agreement between the two.

In this paper, we numerically compare the FMM method with Gaussian beam illumination with the Lorenz-Mie, BEM and FEM methods using plane wave illumination over an evaluation grid of $[-u, u]$ μm. A Gaussian beam needs to have a minimum beam waist radius of approximately u^2 µm in order to have nearly the same amplitude as a plane wave over the evaluation grid. The plane wave and Gaussian amplitude for $u = 3$ μm are shown in Figure 3 (a) and reveal that we only have the same amplitude in a narrow region around the centre of the computational grid. A direct comparison with the Lorenz-Mie, BEM and FEM methods using plane wave illumination is, therefore, only possible in a narrow range around the centre of the computational grid. Figure 3 (b) shows the Gaussian beam amplitude and its angular spectrum representation for the FMM unit cell.

3 Results and discussion

3.1 Single cylinder

In this work, we consider a monochromatic plane electromagnetic wave with a wavelength of 0.5 µm illuminating a silicon cylinder with a radius of 0.5 µm and a refractive index of 4.289 + 0.0489i [78] along the z-axis (see Figure 4(a)). The intensity of the total electric near-field, i.e. the summation of the incident and scattered field from the cylinder in the xz-plane is obtained by the FEM, BEM K-H, BEM M and LFFMM models for both TE and TM polarisations of the incident light. The results are compared with the intensity of the total electric near-field solution of the Mie scattering [79] from a single cylinder with the same specifications and illumination geometry [80]. However, in the LFFMM model, the plane incident wave is approximated by a Gaussian beam with a waist radius of 9 µm to minimise the effect of scattering from the periodic structure. The intensity of the total electric near-field obtained by scattering from the silicon cylinder using the Mie scattering model is shown in Figure 5 for (a) TE and (b) TM polarisation of the incident light over the 2D evaluation grid of [-3, +3] µm in the xz-plane. The sampling distance is set to 10 nm along both the x and z axes. The same evaluation grid and sampling distance are used to simulate the intensity of the total electric field corresponding to the FEM, BEM K-H, BEM M and LFFMM models. Additionally, the amplitude of the incident electromagnetic field is considered as unity for both the Mie and all rigorous models.

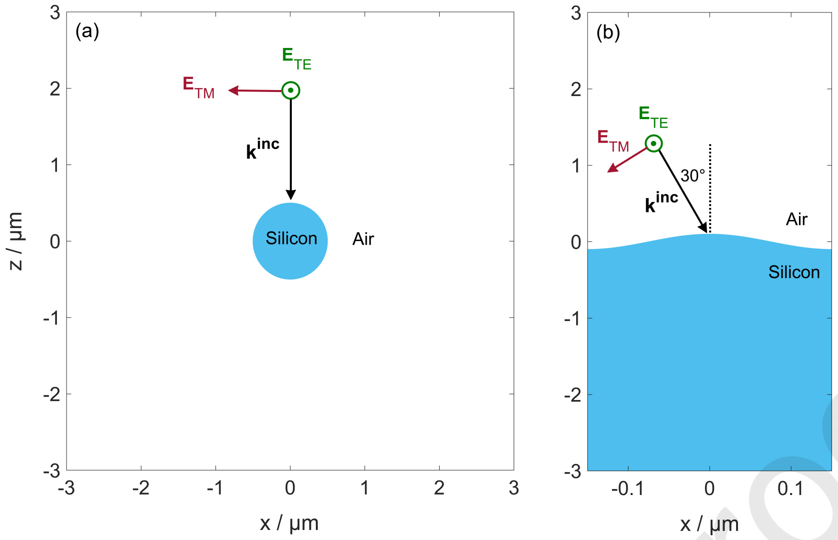

Figure 4: Evaluation grid and illumination geometry for the (a) cylinder and (b) sinusoid profile in the xz-plane. $\mathbf{k}$, $\mathbf{E}_{\mathrm{TE}}$ and $\mathbf{E}_{\mathrm{TM}}$ represent the illumination wave vector, and electric field vectors regarding the TE and TM polarisation, respectively.

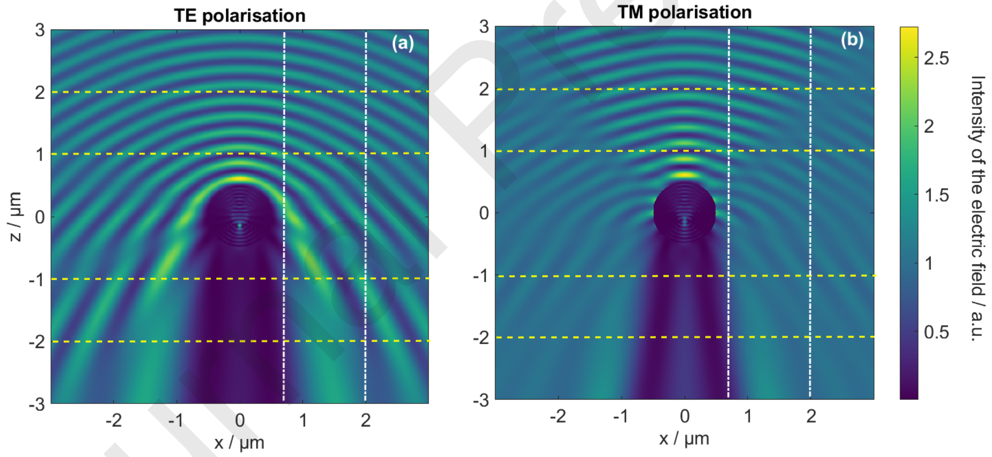

Figure 5: The 2D intensity of the total electric near-field scattered from a silicon cylinder (radius of 0.5 µm and a refractive index of $4.289 + 0.049i$) obtained by the plane wave Mie scattering model for (a) TE and (b) TM polarisation of a monochromatic (wavelength of 0.5 µm) plane wave incident on the cylinder along the -z-axis.

3.1.1 TE mode

Figure 6 shows the 2D difference of the intensity of the electric near-field scattered from the cylinder obtained by the (a) LFFMM, (B) BEM K-H, (c) FEM and (d) BEM M models and the plane wave Mie scattering model for the TE polarisation in the xz-plane. In Figure 6, the colourbar scale is chosen so that more than 99.5 % of the values of the difference between the intensity of the electric field obtained by the presented models and the Mie model fall within the same range. Figure 6 (b) and (c) illustrate that the difference between the intensity of the electric field obtained by the FEM and BEM K-H model and the Mie model is insignificant for the TE polarisation. Figure 6 (a) illustrates that the LFFMM model provides accurate results, specifically in the range of $[-1, +1]$ µm along the x-axis, where the Gaussian and plane wave amplitudes are almost identical. It is important to note that the results beyond this region are not directly comparable to the Mie model due to the substantial impact of amplitude differences between Gaussian and plane waves. Within this limited range, we observe a substantial agreement between the LFFMM and Mie calculations. A closer look reveals the onset of faint periodical areas in the reflection. Our simulation suggests that these spurious modes are caused by the FMM meshing. In this study, the conventional FMM meshing grid, often referred to as staircase approximation, is employed [34]. This grid approximates the cylindrical geometry by using rectangular layers within the Euclidean plane. Circular resonance modes, like whispering gallery modes, cannot propagate as well in the FMM grid since they do not possess the same symmetry as a cylindrical grid. We may, therefore, observe spurious modes by the interaction of resonance modes with the FMM grid.

To quantify the difference between the intensity of the total electric field obtained by each model and the Mie method for the TE polarisation, the mean value of the relative error of the intensity of the total electric field obtained by each model over the evaluated grid of $[-3, +3]$ µm is calculated. Results are shown in Figure 6, and presented in Table 1 (first row). Results indicate that the relative error of the intensity of the total electric field obtained by the FEM, BEM K-H, BEM M and LFFMM models for the TE polarisation across the entire evaluation grid is less than 0.05 %, 0.3 %, 17 % and 12 %, respectively. In the BEM K-H model, elements are represented by source points on the surface. Through surface discretisation, the object's profile is uniformly sampled with a spatial sampling distance of 2.5 nm, resulting in 800 source points on the surface boundary with a maximum Euclidean distance of 0.05 µm ($\lambda/10$) between them. In the BEM M model, the cylinder has a finite length of 15 µm along the y-axis and the edge lengths of the triangular surface elements vary slightly between 0.03 µm and 0.04 µm ($< \lambda/10$). Through additional investigations using different cylinder lengths, we found that a large part of the remaining deviation in the BEM M model result is due to the cylinder's finite length, which induces additional edge effects. In the BEM models, the error in the calculated intensity grows notably along the cylinder's boundary due to the spatial singularity of the Green's function kernel. This, in turn, results in a high relative error in intensity on the boundary when compared to the Mie model, particularly where the source point coincides with the field point. Eliminating the singular points located on the boundary of the cylinder (less than 0.1 % of the total data points) decreases the mean relative error to approximately 0.1 % in the BEM K-H, and 9 % in the BEM M model. In the LFFMM model, restricting the comparison to the evaluation grid of $[-1, +1]$ µm along the x-axis and $[-3, +3]$ µm along the z-axis, reduces the mean relative error to less than 3 %.

Figure 7 shows the intensity profile of the total electric near-field obtained by scattering from the cylinder at (a) $z = -2$ µm, (b) $z = -1$ µm, (c) $z = +2$ µm and (d) $z = +1$ µm along the x-axis (as shown in Figure 5 (a) by the yellow dashed line) using the BEM K-H, BEM M, FEM, LFFMM and Mie models for the TE incidence polarisation. Figure 8 shows the intensity profile of the total electric near-field obtained by scattering from the cylinder at (a) $x = +0.7$ µm, (b) $x = +2$ µm along the z-axis (as shown in Figure 5 (a) by the white dashed-dotted line) using the BEM K-H, BEM M, FEM, LFFMM and Mie models for the TE incidence polarisation. As shown in Figure 7 and 8, the extracted profiles exhibit a strong correspondence among themselves and also with the Mie model. The profiles extracted using the LFFMM model highlight that the dissimilarity between this model and the Mie model increases as the amplitudes of the incident field between them diverge.

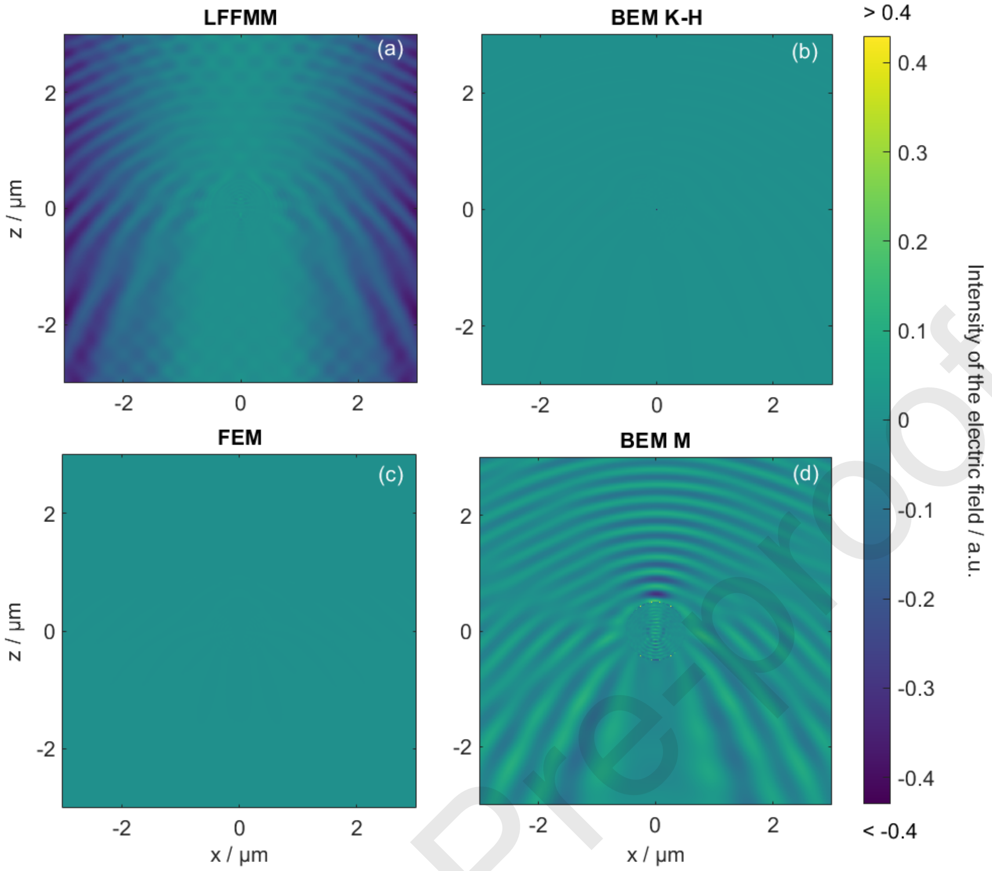

Figure 6: The 2D difference of the intensity of the total electric near-field obtained by scattering from a silicon cylinder using the (a) LFFMM, (b) BEM K-H, (c) FEM and (d) BEM M models and the plane wave Mie scattering model (TE incidence polarisation).

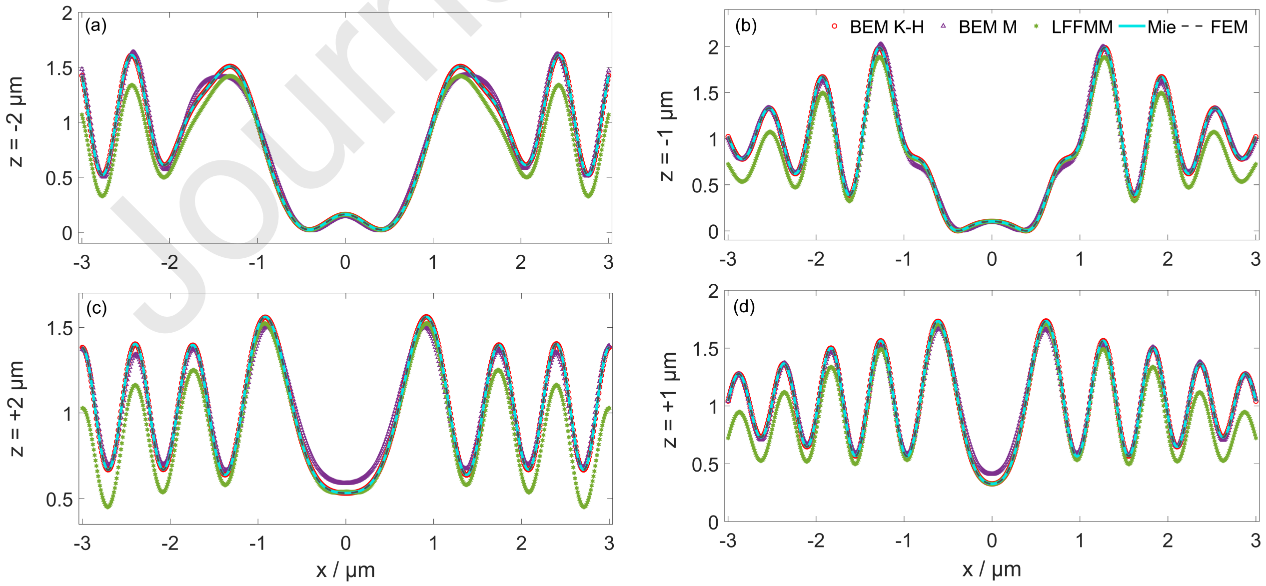

Figure 7: Intensity profile of the total electric near-field obtained by scattering from a silicon cylinder at (a) $z = -2$ μm, (b) $z = -1$ μm, (c) $z = +2$ μm and (d) $z = +1$ μm along the x-axis using the BEM K-H, BEM M, FEM, LFFMM and plane wave Mie models (TE incidence polarisation).

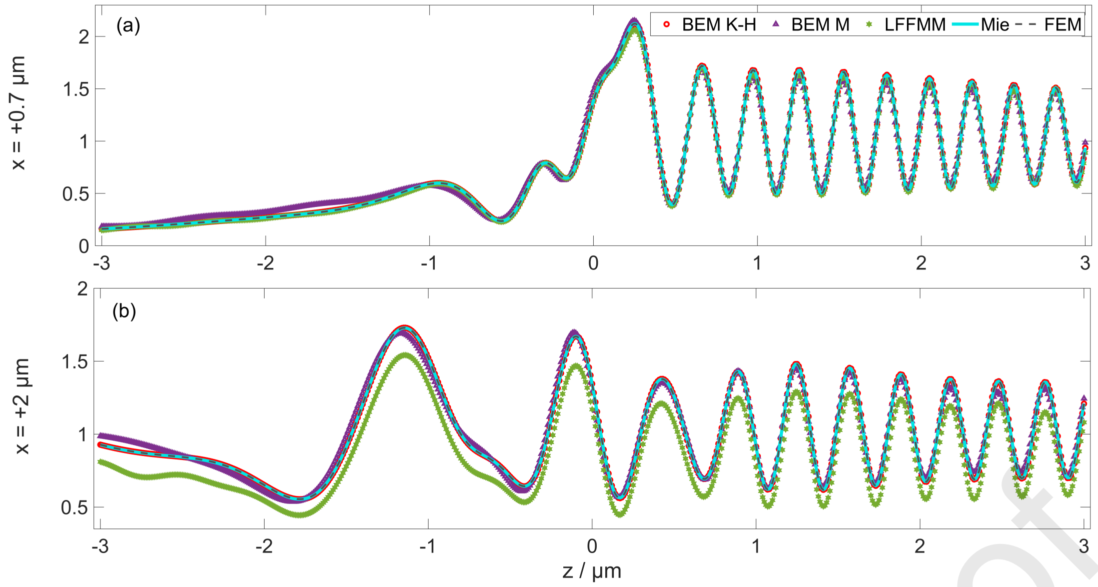

Figure 8: Intensity profile of the total electric near-field obtained by scattering from a silicon cylinder at (a) $x = +0.7$ µm, (b) $x = +2$ µm along the z-axis using the BEM K-H, BEM M, FEM, LFFMM and plane wave Mie models (TE incidence polarisation).

3.1.2 TM mode

Figure 9 shows the 2D difference of the intensity of the electric near-field from the cylinder by the (a) LFFMM, (b) BEM K-H, (c) FEM and (d) BEM M models and the plane wave Mie scattering model for the TM polarisation in the xz-plane. In this figure, the scale of the colourbar is chosen to be similar to that of Figure 6. Hence, one can compare the simulated result obtained by each model for the TE polarisation to that of the TM polarisation.

Figure 9 (c) illustrates that the difference between the intensity of the electric field obtained by the FEM model and the Mie model is insignificant for the TM polarisation. In the BEM K-H model, the object is sampled similarly to the TE mode. However, comparing Figure 6 (b) and Figure 9 (b), it is noticeable that in the BEM K-H model, due to the indirect calculation of the total electric field regarding the TM incidence polarisation, the error in the total electric field is in comparison to the case of TE incidence polarisation. As mentioned in section 2.1, in the BEM K-H model, only the tangential component of the electromagnetic field (H_y) is calculated to fully describe the electromagnetic field in the case of TM polarisation. Therefore, the electric field is obtained indirectly by applying the curl operator to H_y and multiplying the outcome by a factor including the permittivity of the medium through which the light is propagating using Eq. (2). Since the permittivity has different values inside and outside the cylinder, the error of the total electric field is increased at the surface boundary. In the LFFMM model, the electric fields are calculated directly and the magnetic fields are obtained by applying a curl operation. As discussed in 3.1.1, in the LFFMM model, the difference in amplitude of the incident wave over the entire grid, as well as the FMM meshing approach, are the two primary sources contributing to the deviation from the plane wave Mie model. Therefore, more accurate results are expected in the central region along the x-axis. Furthermore, the staircase approximation used in this work causes abrupt permittivity jumps at the meshing boundaries, leading to nonphysical hot spots near the surface boundary. However, the ongoing research indicates that this effect may be significantly reduced when the z-component of the electric field is calculated in Fourier space. This is because the Fourier space approach uses soft boundaries, allowing the external and internal cylindrical fields to cross the structure's boundary. Future studies are anticipated to provide insights into this matter. Figure 9 demonstrates that these hot-spots have a significant influence on the near-field behaviour. Hence, it is evident that the standard FMM meshing method is not able to provide near-field intensity calculations for a cylinder with the same degree of accuracy as the Mie calculations (see the far-field comparison results between the FEM and FMM model in section 6). Therefore, a Fourier space electrical field calculation with more advanced meshing methods, such as adaptive spatial resolution or curvilinear transformations, should be employed to achieve more accurate results in LFFMM concerning cylindrical structures.

To quantify the difference between the intensity of the total electric field obtained by each model and the Mie method for the TM polarisation, the mean value of the relative error of the intensity of the total electric field obtained by each model over the evaluated grid of $[-3, +3]$ µm are calculated and shown in Figure 9. Results are also presented in Table 1 (second row). The results reveal that, for the TM polarisation across the entire evaluation grid of $[-3, +3]$ µm, the relative error of the intensity of the total electric field obtained by the FEM, BEM K-H, BEM M and LFFMM models is approximately 0.06 %, 1 %, 5 % and 13 %, respectively. Removing the singular points located on the boundary of the cylinder (less than 0.1 % of the total data points) decreases the mean relative error to approximately 0.9 % in the BEM K-H, however, it does not significantly change in the BEM M and LFFMM models. In the LFFMM model, restricting the comparison to the evaluation grid of $[-1, +1]$ µm along the x-axis and $[-3, +3]$ µm along the z-axis (the region in which the deviation of incident light amplitude is less than 3 %), reduces the mean relative error to less than 9 %. It is worth mentioning that the relative error of the intensity of the total electric field for all models can be decreased by increasing the number of source points on the surface boundary or decreasing the mesh size, at the cost of increasing the computational time.

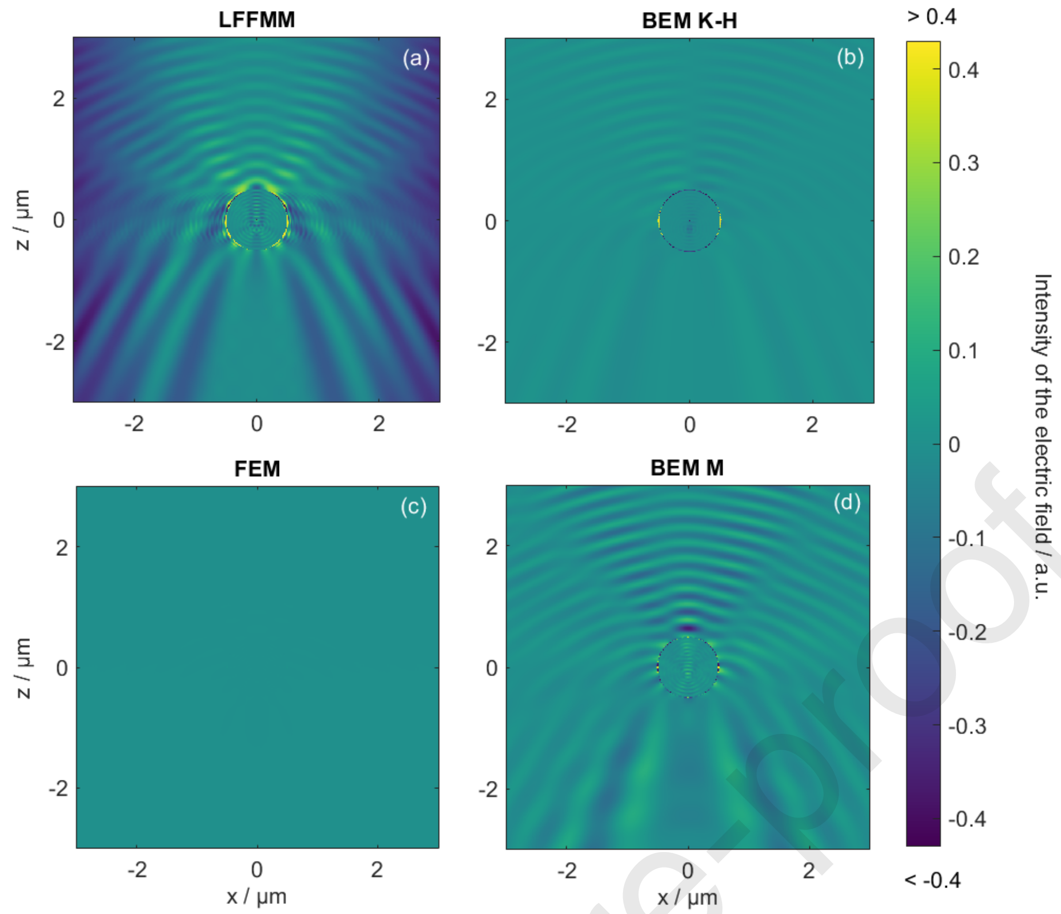

Figure 9: The 2D difference of the intensity of the total electric near-field obtained by scattering from a silicon cylinder using the (a) LFFMM, (b) BEM K-H, (c) FEM and (d) BEM M models and the plane wave Mie scattering model (TM incidence polarisation).

Figure 10 shows the intensity profile of the total electric near-field obtained by scattering from the cylinder at (a) $z = -2$ µm, (b) $z = -1$ µm, (c) $z = +2$ µm and (d) $z = +1$ µm along the x-axis (as shown in Figure 5 (b) by the yellow dashed line) using the BEM K-H, BEM M, FEM, LFFMM and Mie models for the TM incidence polarisation. Figure 11 shows the intensity profile of the total electric near-field obtained by scattering from the cylinder at (a) $x = +0.7$ µm, (b) $x = +2$ µm along the z-axis (as shown in Figure 5 (b) by the white dashed-dotted line) using the BEM K-H, BEM M, FEM, LFFMM and Mie models for the TM incidence polarisation. As illustrated in Figure 10 and 11, the intensity profiles obtained by the FEM, BEM K-H, BEM M and LFFMM (within the central region along the x-axis) models display a significant consistency both among themselves and when compared to the Mie model.

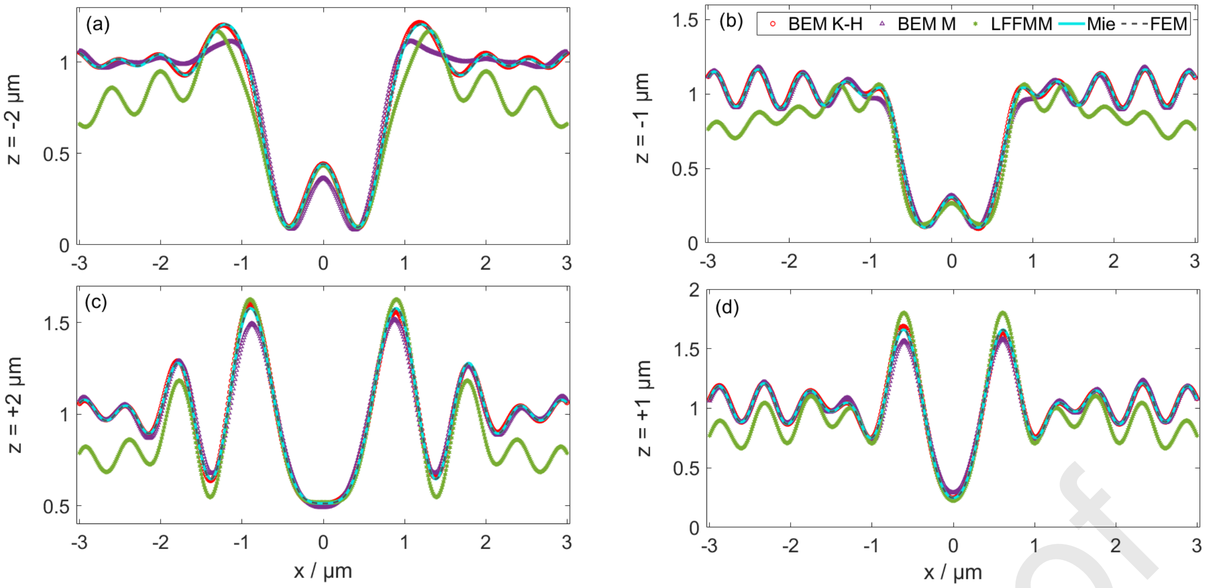

Figure 10: Intensity profile of the total electric near-field obtained by scattering from a silicon cylinder at (a) $z = -2$ µm, (b) $z = -1$ µm, (c) $z = +2$ µm and (d) $z = +1$ µm along the x-axis using the BEM K-H, BEM M, FEM, LFFMM and plane wave Mie models (TM incidence polarisation).

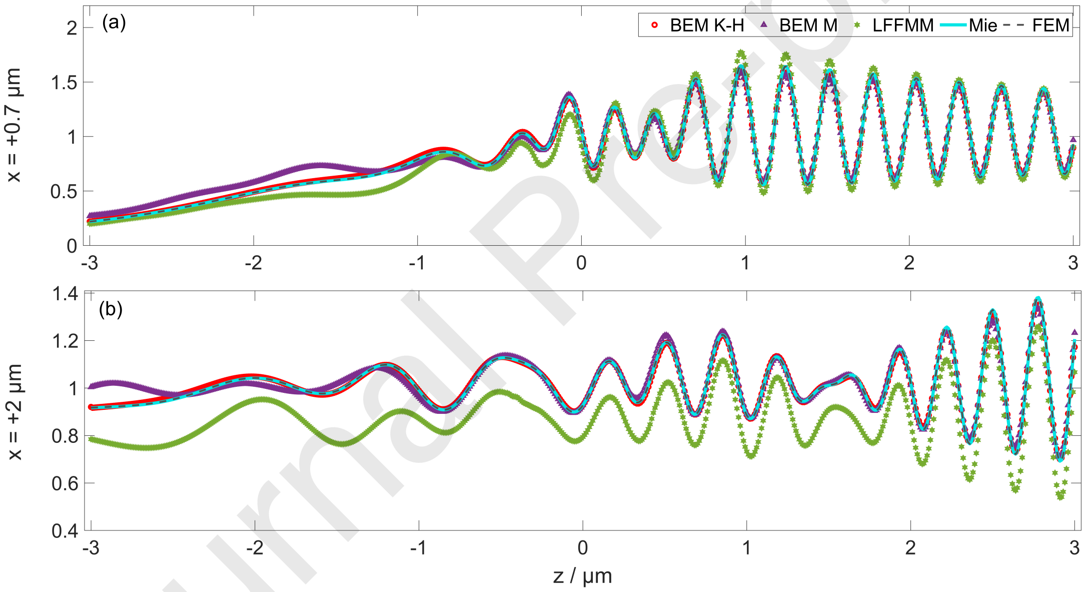

Figure 11: Intensity profile of the total electric near-field obtained by scattering from a silicon cylinder at (a) $x = +0.7$ µm, (b) $x = +2$ µm along the z-axis using the BEM K-H, BEM M, FEM, LFFMM and plane wave Mie models (TM incidence polarisation).

Table 1: Mean value of the relative error of the intensity of the total electric field obtained from the FEM, BEM K-H, BEM M and LFFMM models over the evaluated grid of $[-3, +3]$ µm regarding the TE and TM polarisation of the incident light.

Model / Polarisation	FEM	BEM K-H (raw)	BEM K-H (modified)	BEM M (raw)	BEM M (modified)	LFFMM (raw)	LFFMM (modified)	LFFMM (Gaussian)
TE	0.0004	0.0024	0.0012	0.1687	0.0946	0.1137	0.0260	0.0116
TM	0.0006	0.0111	0.0092	0.0520	0.0502	0.1310	0.0899	0.0556

To demonstrate the influence of the Gaussian amplitude on the difference between the LFFMM model and the plane wave Mie scattering model for the total evaluation grid, a comparison is made between the LFFMM model and the Mie model while the object is illuminated by the Gaussian wave illustrated in Figure 3. Figure 12 shows the 2D difference of the intensity of the total electric near-field, obtained by scattering from the silicon cylinder, using the LFFMM model and the Gaussian Mie model for the (a) TE and (b) TM polarisation of the incident light. The mean relative error between the LFFMM model and the Mie model using the same Gaussian beam is approximately 1 % and 5 % for the TE and TM modes, respectively (see the last column of Table 1). The results illustrate that there is an insignificant error in the intensity of the total electric near-field obtained by the LFFMM model when compared to the Mie model under Gaussian wave illumination.

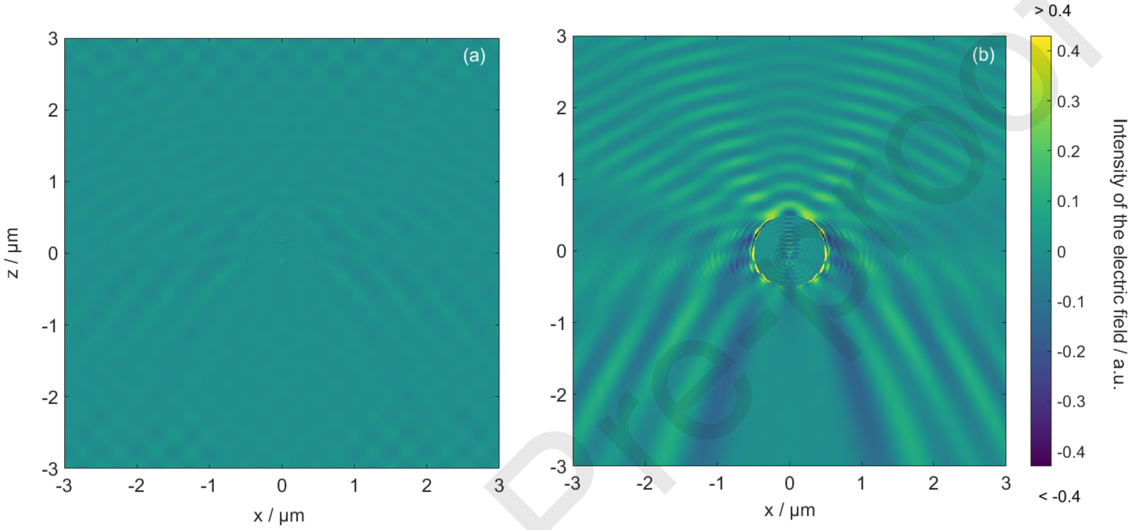

Figure 12: The 2D difference of the intensity of the total electric near-field, obtained by scattering from a silicon cylinder, using the LFFMM and the Mie model while the object is illuminated by the Gaussian wave illustrated in Figure 3, for the (a) TE and (b) TM polarisation of the incident light.

3.2 Sinusoidal profile

To demonstrate the robustness, flexibility and adaptability of the FEM, BEM K-H, BEM M and FMM models, the intensity of the total (near-) electric field obtained by scattering from a periodic object is compared. Consider a monochromatic plane electromagnetic wave with an amplitude of unity and a wavelength of 0.5 µm illuminating a silicon sinusoidal profile at an incident angle of 30° with respect to the -z axis (see Figure 4(b)). The amplitude and pitch value of the sinusoidal profile is considered 0.1 µm and 0.3 µm, respectively, and the object's refractive index is $4.289 + 0.0489i$. The maximum slope angle of the sinusoidal profile ($\approx 65°$) is chosen so that only a rigorous model can predict the scattered light. The intensity of the total electric near-field scattered from the sinusoidal profile in the xz-plane is obtained by the FEM, BEM K-H, BEM M and FMM models for the TE and TM polarisation of the incident light. In the BEM K-H model, similar to the single cylinder case, elements are represented by source points on the surface. Through surface discretisation, the object's profile is uniformly sampled with a spatial sampling distance of 39 nm, resulting in a maximum Euclidean distance of 0.05 µm ($\lambda/10$) between the source points. In the BEM K-H and BEM M models, the profile is considered quasi-periodic since a sine wave is extended over 100 and 55 cycles, respectively. For the BEM M 3D model, the sinusoidal grating has a finite depth of 3 µm along the y axis.

3.2.1 TE mode

The intensity of the total electric near-field obtained by scattering from the sinusoidal profile for the TE polarisation of the incident light is shown in Figure 13 using the (a) FEM, (b) BEM K-H, (c) BEM M and (d) FMM, over the 2D evaluation grid of [-0.15, +0.15] µm along the x-axis and [-2, +2] µm along the z-axis. The sampling distance is set to 2 nm along both the x and z axes.

Figure 14 shows the intensity profile of the total electric near-field obtained by scattering from a sinusoidal profile at (a) z = +0.5 µm, (b) z = -0.5 µm, (c) z = +1.5 µm and (d) z= -1.5 µm along the x-axis using the BEM K-H, BEM M, FEM and FMM models for the TE incidence polarisation. Figure 15 shows the intensity profile of the total electric near-field obtained scattering from a sinusoidal profile at (a) x = +0.05 µm, (b) x = -0.05 µm, (c) x = +0.1 µm and (d) x = -0.1 µm along the z-axis using the BEM K-H, BEM M, FEM and FMM models for the TE incidence polarisation.

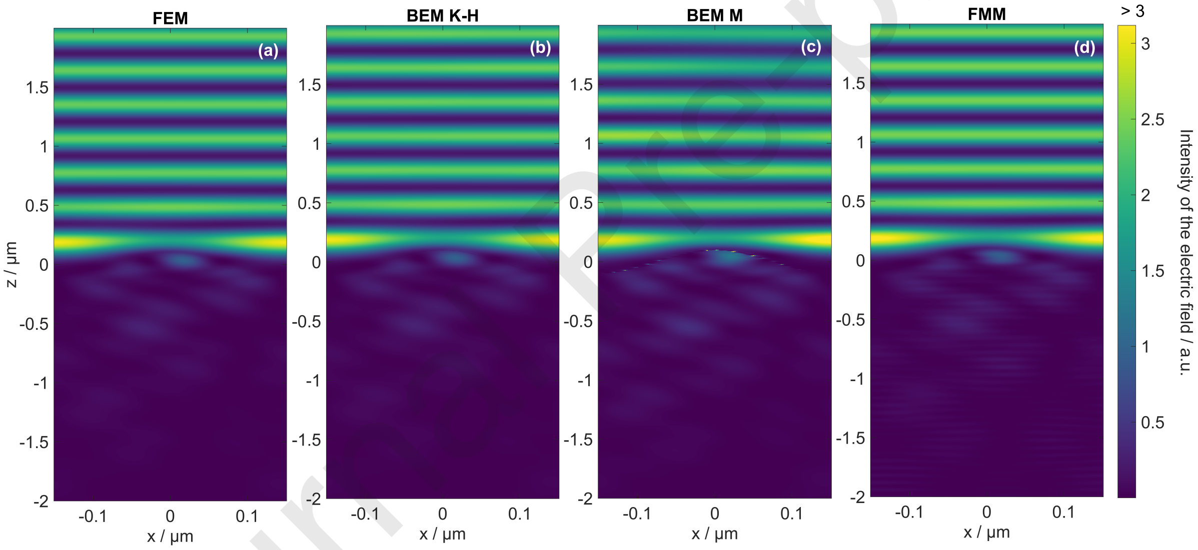

Figure 13: The 2D intensity of the total electric near-field obtained by scattering from the sinusoidal profile for the TE polarisation of the incident light using the (a) FEM, (b) BEM K-H, (c) BEM M and (d) FMM models in the xz-plane.

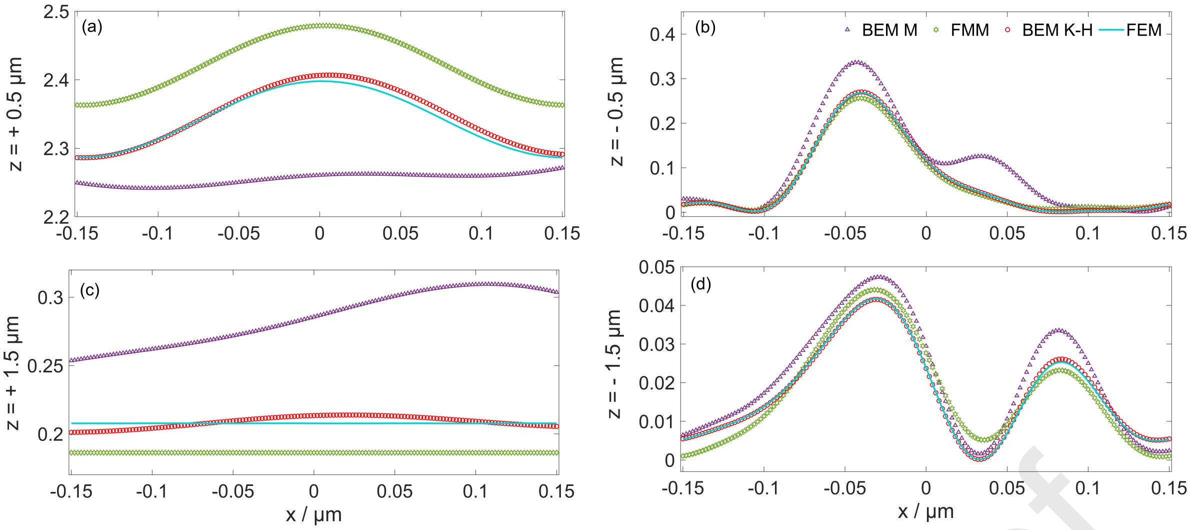

Figure 14: Intensity profile of the total electric near-field obtained by scattering from a sinusoidal profile at (a) z = +0.5 μm, (b) z = -0.5 μm, (c) z = +1.5 μm and (d) z= -1.5 μm along the x-axis using the BEM K-H, BEM M, FEM and FMM models (TE incidence polarisation).

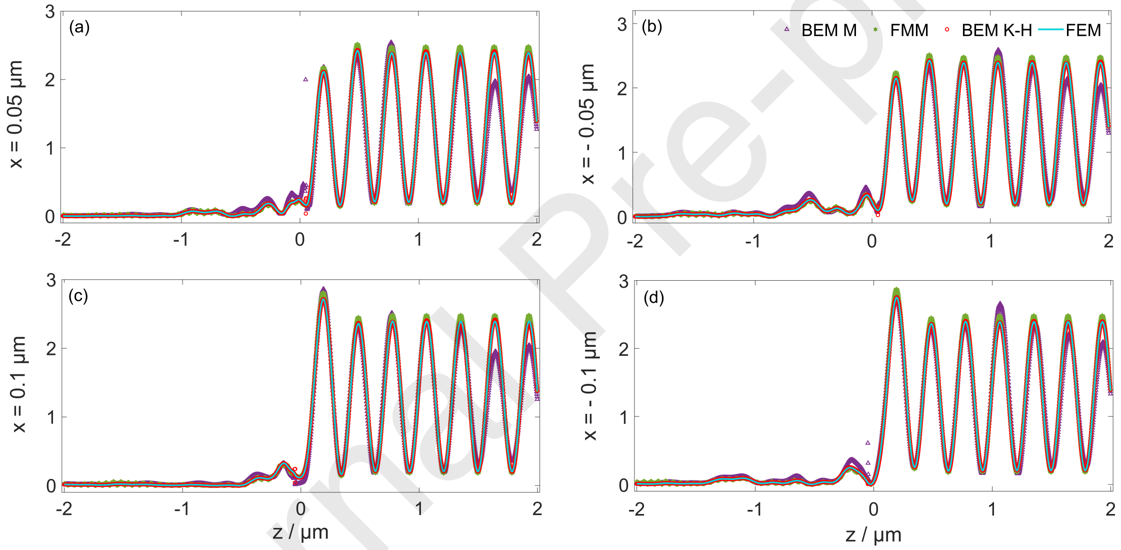

Figure 15: Intensity profile of the total electric near-field obtained by scattering from a sinusoidal profile at (a) x = +0.05 μm, (b) x = -0.05 μm, (c) x = +0.1 μm and (d) x = -0.1 μm along the z-axis using the BEM K-H, BEM M, FEM and FMM models (TE incidence polarisation).

3.2.2 TM mode

The intensity of the total electric near-field obtained by scattering from the sinusoidal profile for the TM polarisation of the incident light is shown in Figure 16 using the (a) FEM, (b) BEM K-H, (c) BEM M and (d) FMM models, over the same evaluation grid and sampling distance along the x and z axes as considered in the TM polarisation case.

Figure 17 shows the intensity profile of the total electric near-field obtained by scattering from a sinusoidal profile at (a) z = +0.5 μm, (b) z = -0.5 μm, (c) z = +1.5 μm and (d) z= -1.5 μm along the x-axis using the BEM K-H, BEM M, FEM and FMM models for the TM incidence polarisation. Figure 18 shows the intensity profile of the total electric near-field obtained scattering from a sinusoidal profile at (a) x = +0.05 μm, (b) x = -0.05 μm, (c) x

= +0.1 µm and (d) x = -0.1 µm along the z-axis using the BEM K-H, BEM M, FEM and FMM models for the TM incidence polarisation. Figures 13 to 18 demonstrates a significant agreement in the intensity of the total electric field scattered from the sinusoidal profile in the xz-plane, obtained by the FEM, BEM K-H, BEM M, and FMM models, for both TE and TM polarisations of the incident light. The mean value of the difference between the intensities of the extracted profiles of figures 14, 15, 17 and 18, obtained by each pair of models, is within the range of 0.0003 a.u. and 0.09 a.u. for both TE and TM polarisations. This agreement illustrates the capability of these models to accurately assess scattered light from profiles characterised by high slope angles.

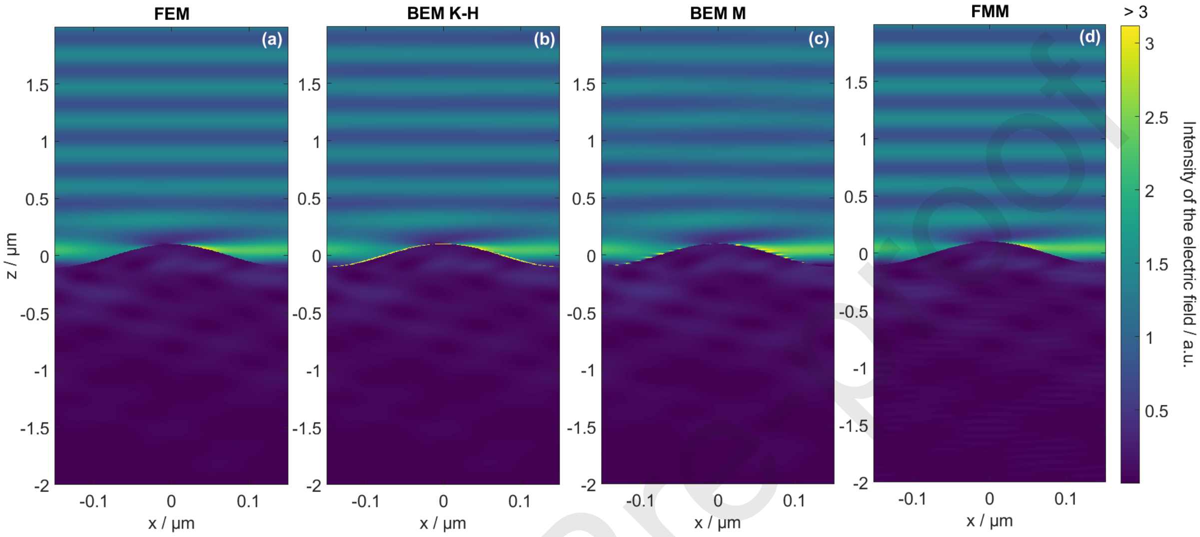

Figure 16: The 2D intensity of the total electric near-field obtained by scattering from the sinusoidal profile for the TM polarisation of the incident light using the (a) FEM, (b) BEM K-H, (c) BEM M and (d) FMM models in the xz-plane.

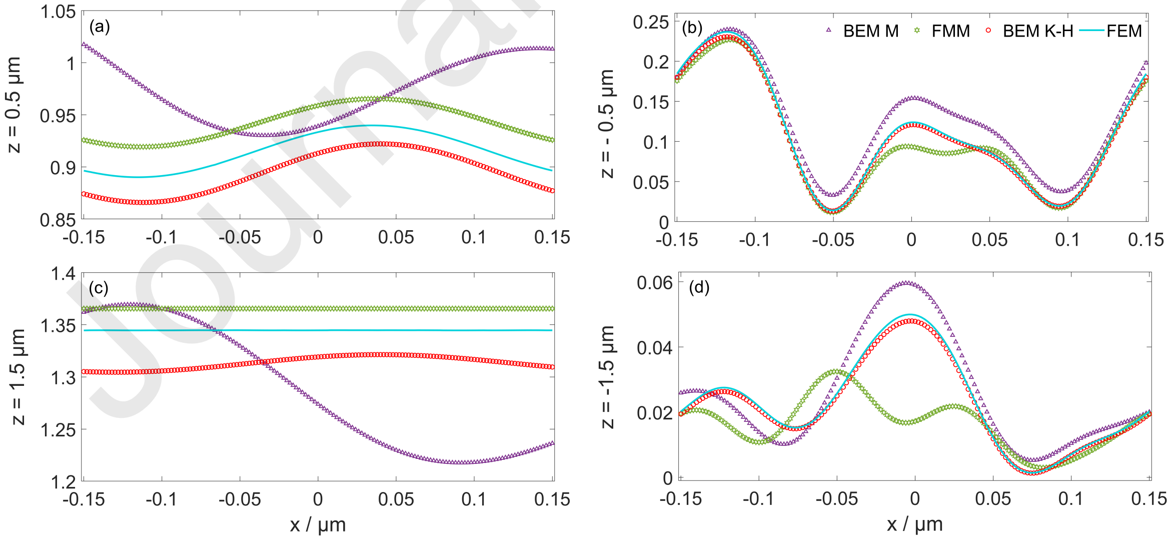

Figure 17: Intensity profile of the total electric near-field obtained by scattering from a sinusoidal profile at (a) z = +0.5 µm, (b) z = -0.5 µm, (c) z = +1.5 µm and (d) z= -1.5 µm along the x-axis using the BEM K-H, BEM M, FEM and FMM models (TM incidence polarisation).

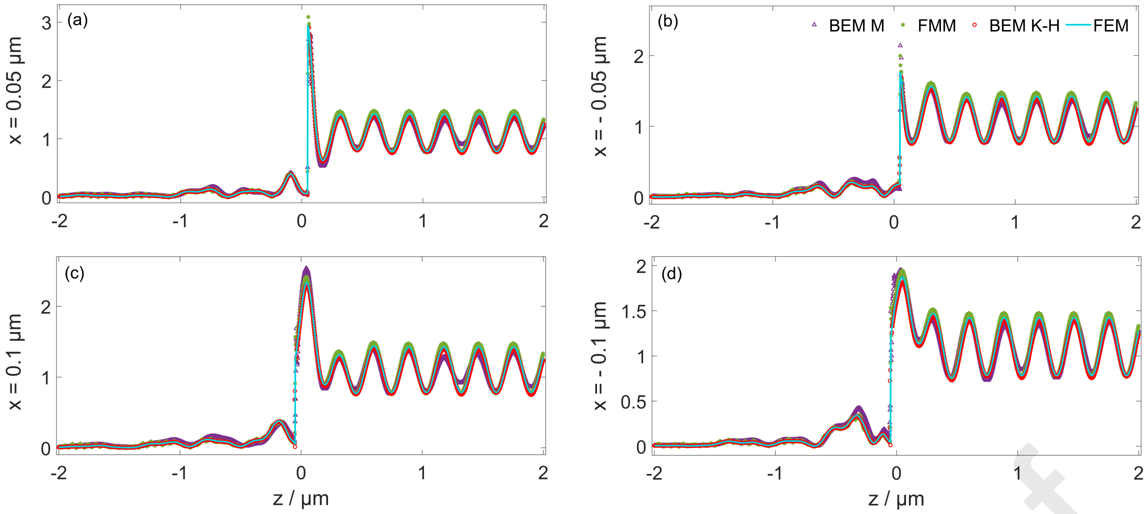

Figure 18: Intensity profile of the total electric near-field obtained by scattering from a sinusoidal profile at (a) x = +0.05 µm, (b) x = -0.05 µm, (c) x = +0.1 µm and (d) x = -0.1 µm along the z-axis using the BEM K-H, BEM M, FEM and FMM models (TM incidence polarisation).

4 Conclusion

Due to the increasing use of freeform surfaces, surfaces with technologically advanced texturing, and additively manufactured structures in engineering, the aerospace industry and biology, analysing the complex features on the surface is becoming more critical. Rigorous scattering models have thus been widely developed to predict the scattered light from complex surface geometries including overhangs and re-entrant features, where multiple scattering is inevitable.

In this paper, the intensity of the total electric near-field scattered from a silicon cylinder of the radius of 0.5 µm and a refractive index of $4.289{+}0.0489i$ is simulated using four different rigorous models based on Maxwell's equations including the FEM, two approaches based on the BEM method (BEM K-H and BEM M) and the LFFMM method. The cylinder is illuminated by a monochromatic plane electromagnetic wave with a wavelength of 0.5 µm along the -z axis, and both the TE and TM polarisations are considered for the incident light. In the LFFMM model, the periodic FMM structure is transformed into a single structure using a localised Gaussian input field. The intensity of the total electric field obtained by these models is compared using the Mie solution as a reference over the evaluation grid of [-3, +3] µm in the xz-plane.

The results demonstrate strong agreement between the FEM, BEM K-H, BEM M, and LFFMM models with Mie solutions for both TE and TM polarisations, confirming their accuracy in simulating near-field scattering. FEM achieved a mean relative error of less than 0.1 % for both polarisations but is computationally intensive. The BEM K-H model, while maintaining accuracy (0.1 % error for TE, 0.9 % for TM), is faster and more efficient as a 2D method. The BEM M model showed a higher error (5 % for TM, 10 % for TE) but is more powerful for treating surfaces with 3D profiles. LFFMM, while less accurate (3 % error for TE, 9 % for TM), overcomes periodicity limitations with Gaussian illumination. It should be noted that LFFMM is a newly developed rigorous scattering technique that employs localised fields instead of PML layers. As a newly developed method, there is room for improvement, and ongoing efforts are being made to enhance its performance.

To assess the robustness, flexibility, and adaptability of the rigorous models, the intensity of the scattered field from a periodic silicon sinusoidal profile is analyzed. A monochromatic plane wave with a 0.5 µm wavelength illuminates the profile at a 30° angle to the z-axis. The profile has an amplitude of 0.1 µm, a pitch of 0.3 µm, and a refractive index of $4.289 + 0.0489i$. The maximum slope angle of the profile is approximately 65 degrees, requiring a rigorous model to predict the scattered light. The mean difference in the total electric near-field intensity scattered from the sinusoidal profile, as calculated by the FEM, BEM K-H, BEM M, and FMM models along various vertical and horizontal lines in the xz-plane, ranges between 0.0003 a.u. and 0.09 a.u. for both TE and TM polarisations, assuming the amplitude of the incident electromagnetic field is unity for all rigorous models. This highlights the models' effectiveness in evaluating scattered light from complex profiles.

We have shown that the four models, all based on different methods, yield consistent results. This result suggests that each one is viable for solving real-world problems where a rigorous scattering model is needed. Each model offers its own set of advantages, so the choice between them should be made depending on the specific requirements of the application.

5 Author contribution

Helia Hooshmand: Implementation, simulation and writing of text about the BEM K-H model. Analysis and interpretation of the results and manuscript preparation.
Poul-Erik Hansen: Idea, theory and implementation of LFFMM method and simulation of the two structures. Writing the article section on aperiodic LFFMM.
Mirza Karamehmedović: Support of the LFFMM method.
Liwei Fu: Implementation of BEM M method and simulation of the two structures.
Alexander Birk: Support of the BEM M simulation. Writing the article section on the method and results of BEM M.
Tobias Pahl: Implementation, simulation and writing of text about FEM.
Stephan Reichelt, Richard Leach, Peter Lehmann and Samanta Piano: Supervision and review.

Disclosures

The authors declare no conflicts of interest.

Data availability

The data obtained and used in this contribution can be provided by the corresponding author upon request. The data will also be uploaded to the Zenodo database after acceptance.

Funding

This research work was partially funded by the European Metrology Programme for Innovation and Research (EMPIR) project [TracOptic, 20IND07]. Helia Hooshmand was supported by the European Union [ERC, AI-SURF, 101054454] and would like to thank the UKRI Research England Development (RED) Fund for supporting this work via the Midlands Centre for Data-Driven Metrology. P.-E. Hansen was also supported by the Danish Agency for Institutions and Education, the EUREKA project E13241-NanoMeas grant funded by Innovation Fund Denmark and the EMPIR program (project POLight, 20FUN02) co-financed by the Participating States and from the European Union's Horizon 2020 research and innovation program. Tobias Pahl was funded by the German Research Foundation [DFG, LE992/14-3].

References

1. Ho, P. & Weiner, J. *Light-Matter Interaction: Fundamentals and Applications* **v. 1** (Wiley, 2008).
2. Stenzel, O. *Light–Matter Interaction: A Crash Course for Students of Optics, Photonics and Materials Science* (Springer International Publishing, 2022).
3. Townsend, A., Senin, N., Blunt, L., Leach, R. & Taylor, J. Surface texture metrology for metal additive manufacturing: a review. *Precision Engineering* **46,** 34–47 (2016).
4. Catalucci, S., Thompson, A., Piano, S., Branson III, D. T. & Leach, R. K. Optical metrology for digital manufacturing: a review. *The International Journal of Advanced Manufacturing Technology* **120,** 4271–4290 (2022).
5. Catalucci, S. *et al.* Smart optical coordinate and surface metrology. *Measurement Science and Technology* **34,** 012001 (2022).
6. Leach, R. K. *Advances in Optical Surface Texture Metrology* ISBN: 9780750325264. `https://books.google.co.uk/books?id=gnwZxQEACAAJ` (IOP PUBL Limited, 2020).
7. De Groot, P. J. & Colonna de Lega, X. Fourier optics modeling of interference microscopes. *Journal of the Optical Society of America A* **37,** B1–B10. `http://opg.optica.org/josaa/abstract.cfm?URI=josaa-37-9-B1` (2020).
8. *ISO 25178 Part 600* Geometrical product specifications (GPS) — Surface texture: Areal, Metrological characteristics for areal topography measuring methods (International Organization for Standardization, Geneva, CH, 2019).
9. De Groot, P. J., Kramer, J. W. & Sutherland, T. P. *Modeling the topographic lateral resolution of interferometers* in *Modeling Aspects in Optical Metrology IX* (eds Bodermann, B. & Frenner, K.) **12619** (SPIE, 2023), 126190N. `https://doi.org/10.1117/12.2670939`.
10. De Groot, P. J. The instrument transfer function for optical measurements of surface topography. *Journal of Physics: Photonics* **3,** 024004. `https://dx.doi.org/10.1088/2515-7647/abe3da` (Feb. 2021).
11. De Groot, P. J. & de Lega, X. C. Fourier optics modeling of interference microscopes. *J. Opt. Soc. Am. A* **37,** B1–B10 (2020).
12. Coupland, J., Mandal, R., Palodhi, K. & Leach, R. K. Coherence scanning interferometry: linear theory of surface measurement. *Appl. Opt.* **52,** 3662–3670 (2013).
13. Lehmann, P., Hüser, L., Stelter, A. & Kusserow, T. Lateral resolution enhanced interference microscopy using virtual annular apertures. *Journal of Physics: Photonics* **5,** 015001 (2023).
14. Hooshmand, H. *et al.* Comparison of Fourier optics-based methods for modeling coherence scanning interferometry. *Optical Engineering* **63,** 044102. `https://doi.org/10.1117/1.OE.63.4.044102` (2024).
15. Hooshmand, H., Liu, M., Leach, R. K. & Piano, S. Quantitative investigation of the validity conditions for the Beckmann–Kirchhoff scattering model. *Optical Engineering* **61,** 124113 (2022).
16. Khan, M. & Jappes, J. *Innovations in Additive Manufacturing* (Springer International Publishing, 2022).
17. Born, M. & Wolf, E. *Principles of Optics: Electromagnetic Theory of Propagation, Interference and Diffraction of Light* (Elsevier Science, 2013).
18. Jackson, J. *Classical Electrodynamics* (John Wiley & Sons, New York, 2021).
19. Jin, J. *The Finite Element Method in Electromagnetics* (Wiley, 2015).
20. Kim, H., Park, J. & Lee, B. *Fourier Modal Method and Its Applications in Computational Nanophotonics* (CRC Press, 2017).
21. Jarem, J. & Banerjee, P. *Computational Methods for Electromagnetic and Optical Systems, Second Edition* (Taylor & Francis, 2011).
22. Moharam, M. G. & Gaylord, T. K. Rigorous coupled-wave analysis of planar-grating diffraction. *J. Opt. Soc. Am.* **71,** 811–818 (1981).
23. Watanabe, K., Pištora, J. & Nakatake, Y. Rigorous coupled-wave analysis of electromagnetic scattering from lamellar grating with defects. *Opt. Express* **19,** 25799–25811 (2011).

24. Kunz, K. & Luebbers, R. *The Finite Difference Time Domain Method for Electromagnetics* (Taylor & Francis Limited (Sales), 2019).
25. Coomar, A., Arntsen, C., Lopata, K. A., Pistinner, S. & Neuhauser, D. Near-field: A finite-difference time-dependent method for simulation of electrodynamics on small scales. *The Journal of Chemical Physics* **135,** 084121 (2011).
26. Tsukerman, I. in *Computational Methods for Nanoscale Applications: Particles, Plasmons and Waves* 357–423 (Springer International Publishing, Cham, 2020).
27. Fu, L., Frenner, K. & Osten, W. Rigorous speckle simulation using surface integral equations and higher order boundary element method. *Opt. Lett.* **39,** 4104–4107 (2014).
28. Simonsen, I. Optics of surface disordered systems. *The European Physical Journal Special Topics* **181,** 1–103 (2010).
29. Fairweather, G. & Karageorghis, A. The method of fundamental solutions for elliptic boundary value problems. *Advances in Computational Mathematics* **9,** 69–95 (1998).
30. Fairweather, G., Karageorghis, A. & Martin, P. A. The method of fundamental solutions for scattering and radiation problems. *Engineering Analysis with Boundary Elements* **27,** 759–769 (2003).
31. Doicu, A., Eremin, Y. A. & Wriedt, T. *Acoustic and Electromagnetic Scattering Analysis Using Discrete Sources* (Academic Press, 2000).
32. Wriedt, T. *Generalized Multipole Techniques for Electromagnetic and Light Scattering* (Elsevier, 1999).
33. Karamehmedović, M., Sørensen, M.-P., Hansen, P.-E. & Lavrinenko, A. V. Application of the method of auxiliary sources to a defect-detection inverse problem of optical diffraction microscopy. *Journal of the European Optical Society – Rapid Publications* **5** (2010).
34. Madsen, M. H. & Hansen, P.-E. Scatterometry—fast and robust measurements of nano-textured surfaces. *Surface Topography: Metrology and Properties* **4,** 023003 (2016).
35. Gross, H. *et al.* Mathematical modelling of indirect measurements in scatterometry. *Measurement* **39,** 782–794 (2006).
36. Fu, L., Daiber-Huppert, M., Frenner, K. & Osten, W. Simulation of realistic speckle fields by using surface integral equation and multi-level fast multipole method. *Optics and Lasers in Engineering* **162,** 107438 (2023).
37. Pahl, T., Hagemeier, S., Künne, M., Yang, D. & Lehmann, P. 3D modeling of coherence scanning interferometry on 2D surfaces using FEM. *Optics Express* **28,** 39807–39826 (2020).
38. Thomas, M., Su, R., Nikolaev, N., Coupland, J. & Leach, R. K. Modeling of interference microscopy beyond the linear regime. *Optical Engineering* **59,** 034110. `https://doi.org/10.1117/1.OE.59.3.034110` (2020).
39. Pahl, T., Hagemeier, S., Bischoff, J., Manske, E. & Lehmann, P. Rigorous 3D modeling of confocal microscopy on 2D surface topographies. *Measurement Science and Technology* **32,** 094010 (2021).
40. Pahl, T., Hüser, L., Hagemeier, S. & Lehmann, P. FEM-based modeling of microsphere-enhanced interferometry. *Light: Advanced Manufacturing* **3,** 1–13 (2022).
41. Pahl, T., Hagemeier, S., Hüser, L., Rosenthal, F. & Lehmann, P. Simulative investigation of microcylinder-assisted microscopy in reflection and transmission mode. *Proc. SPIE* **12619,** 126190K (2023).
42. Thomas, M., Su, R., de Groot, P., Coupland, J. & Leach, R. K. Surface measuring coherence scanning interferometry beyond the specular reflection limit. *Opt. Express* **29,** 36121–36131 (2021).
43. Lalanne, P. *et al.* Numerical analysis of a slit-groove diffraction problem. *Journal of the European Optical Society - Rapid publications* **2** (2007).
44. Karamehmedović, M. *et al.* Comparison of numerical methods in near-field computation for metallic nanoparticles. *Optics Express* **19** (2011).
45. Davidson, M. P., Kleemann, B. H. & Bischoff, J. *Comparison between rigorous light-scattering methods* in *Optical Microlithography X* (ed Fuller, G. E.) **3051** (SPIE, 1997), 606–619.

46. Anttu, N. *et al.* Comparison of absorption simulation in semiconductor nanowire and nanocone arrays with the Fourier modal method, the finite element method, and the finite-difference time-domain method. *Nano Express* **1,** 030034.
47. Solano, M. E., Faryad, M., Lakhtakia, A. & Monk, P. B. Comparison of rigorous coupled-wave approach and finite element method for photovoltaic devices with periodically corrugated metallic backreflector. *J. Opt. Soc. Am. A* **31,** 2275–2284 (2014).
48. Su, R. *et al.* Lens aberration compensation in interference microscopy. *Optics and Lasers in Engineering* **128,** 106015. ISSN: 0143-8166. https://www.sciencedirect.com/science/article/pii/S014381661931303X (2020).
49. Maradudin, A. A., Michel, T., McGurn, A. R. & Méndez, E. R. Enhanced backscattering of light from a random grating. *Annals of Physics* **203,** 255–307 (1990).
50. Born, M. & Wolf, E. *Principles of Optics: Electromagnetic Theory of Propagation, Interference and Diffraction of Light* (Cambridge University Press, Cambridge, 1999).
51. Kong, J. *Electromagnetic Wave Theory* (EMW Publishing, Cambridge, 2000).
52. Beckmann, P. & Spizzichino, A. *The Scattering of Electromagnetic Waves from Rough Surfaces* (Artech House, Norwood, MA, 1987).
53. Abramowitz, M. & Stegun, I. *Handbook of Mathematical Functions: with Formulas, Graphs, and Mathematical Tables* (Dover Publications, New York, 2012).
54. Wolf, E. *A Generalized Extinction Theorem and Its Role in Scattering Theory* in *Coherence and Quantum Optics* (eds Mandel, L. & Wolf, E.) (Springer US, Boston, MA, 1973), 339–357.
55. Harrington, R. *Field Computation by Moment Methods* (John Wiley & Sons, New York, 1993).
56. Stratton, J. A. & Chu, L. J. Diffraction Theory of Electromagnetic Waves. *Phys. Rev.* **56,** 99–107 (1 1939).
57. Medgyesi-Mitschang, L. N., Putnam, J. M. & Gedera, M. B. Generalized method of moments for three-dimensional penetrable scatterers. *J. Opt. Soc. Am. A* **11,** 1383–1398 (1994).
58. Greengard, L. & Rokhlin, V. A fast algorithm for particle simulations. English (US). *Journal of Computational Physics* **135,** 280–292 (1987).
59. Song, J., Lu, C.-C. & Chew, W. C. Multilevel fast multipole algorithm for electromagnetic scattering by large complex objects. *IEEE Transactions on Antennas and Propagation* **45,** 1488–1493. ISSN: 0018-926X (1997).
60. Saad, Y. & Schultz, M. H. GMRES: A Generalized Minimal Residual Algorithm for Solving Nonsymmetric Linear Systems. *SIAM Journal on Scientific and Statistical Computing* **7,** 856–869 (1986).
61. Jin, J. M. *The finite element method in electromagnetics* 3rd ed. (John Wiley & Sons, New York, 2015).
62. Volakis, J., Chatterjee, A. & Kempel, L. *Finite element method for electromagnetics: antennas, microwave circuits, and scattering applications* (John Wiley & Sons, New York, 1998).
63. Pahl, T., Hagemeier, S., Hüser, L., Xie, W. & Lehmann, P. Two-dimensional modeling of systematic surface height deviations in optical interference microscopy based on rigorous near field calculation. *Journal of Modern Optics* **67,** 963–973 (2020).
64. Sacks, Z. S., Kingsland, D. M., Lee, R. & Lee, J.-F. A perfectly matched anisotropic absorber for use as an absorbing boundary condition. *IEEE transactions on Antennas and Propagation* **43,** 1460–1463 (1995).
65. *NGSolve* https://ngsolve.org/. 2022.
66. Logg, A., Mardal, K. & Wells, G. *Automated solution of differential equations by the finite element method: The FEniCS book* (Springer Science & Business Media, Berlin, 2012).
67. Wu, S.-D., Gaylord, T. K., Glytsis, E. N. & Wu, Y.-M. Three-dimensional converging–diverging Gaussian beam diffraction by a volume grating. *J. Opt. Soc. Am. A* **22,** 1293–1303 (2005).

68. Ma, Z., Hansen, P.-E., Wang, H., Karamehmedović, M. & Chen, Q. Harvey Schack theory for converging-diverging Gaussian beam. *J. Opt. Soc. Am. B* (2023).

69. Novotny, L. & Hecht, B. *Principles of Nano-Optics: electromagnetic theory of propagation, interference and diffraction of light* 2th ed. ISBN: 9780511794193 (Cambridge University Press, New York, 2012).

70. Hansen, P.-E., Madsen, M. H., Lehtolahti, J. & Nielsen, L. Traceable Mueller polarimetry and scatterometry for shape reconstruction of grating structures. *Applied Surface Science* **421.** 7'th International Conference on Spectroscopic Ellipsometry, 471–479 (2017).

71. Rumpf, R. C. Improved Formulation of Scattering Matrices for Semi-Analytical Methods That Is Consistent with Convention. *Progress In Electromagnetics Research B* **35,** 241–261 (2011).

72. Moharam, M. G., Pommet, D. A., Grann, E. B. & Gaylord, T. K. Stable implementation of the rigorous coupled-wave analysis for surface-relief gratings: enhanced transmittance matrix approach. *J. Opt. Soc. Am. A* **12,** 1077–1086 (1995).

73. Weismann, M., Gallagher, D. F. G. & Panoiu, N. C. Accurate near-field calculation in the rigorous coupled-wave analysis method. *Journal of Optics* **17,** 125612 (2015).

74. Lyaschuk, Y. M., Kukhtaruk, S. M., Janonis, V. & Korotyeyev, V. V. Modified rigorous coupled-wave analysis for grating-based plasmonic structures with a delta-thin conductive channel: far- and near-field study. *J. Opt. Soc. Am. A* **38,** 157–167 (2021).

75. Kim, H., Park, J. & Lee, B. *Fourier Modal Method and Its Applications in Computational Nanophotonics* 1th ed (CRC Press, 2012).

76. Pisarenco, M., Maubach, J., Setija, I. & Mattheij, R. Aperiodic Fourier modal method in contrast-field formulation for simulation of scattering from finite structures. *J. Opt. Soc. Am. A* **27,** 2423–2431 (2010).

77. Rook, R., Pisarenco, M. & Setija, I. D. Near- to far-field transformation in the aperiodic Fourier modal method. *Appl. Opt.* **52,** 6962–6968 (2013).

78. Schinke, C. *et al.* Uncertainty analysis for the coefficient of band-to-band absorption of crystalline silicon. *Aip Advances* **5** (2015).

79. Bohren, C. & Huffman, D. *Absorption and Scattering of Light by Small Particles* (Wiley, 1983).

80. Schäfer, J., Lee, S.-C. & Kienle, A. Calculation of the near fields for the scattering of electromagnetic waves by multiple infinite cylinders at perpendicular incidence. *Journal of Quantitative Spectroscopy and Radiative Transfer* **113,** 2113–2123 (2012).

Declaration of interests

☒ The authors declare that they have no known competing financial interests or personal relationships that could have appeared to influence the work reported in this paper.

☐ The authors declare the following financial interests/personal relationships which may be considered as potential competing interests: